# Contact Modeling in the Discrete Element Method


**Jerzy Rojek**

**Abstract** The discrete element method (DEM) is a wide family of numerical methods for discrete and discontinuous modelling of materials and systems which can be represented by a large collection of particles (discrete elements). The DEM assumes that the discrete elements interact with one another by contact forces. This chapter presents basic aspects of contact modeling in the DEM. The main assumptions, theoretical formulation and numerical algorithm of the DEM are presented. In this work, the DEM formulation employing spherical particles and the soft-contact approach is considered. Basic contact models for the particle interaction are reviewed. Elementary contact mechanisms, including elasticity, plasticity, damping, friction and cohesion are discussed. Selected contact models combining these effects are described. Their performance in modelling single dynamic or quasi-static contact events is analysed. The analysis is focused on the evolution of contact forces during single collisions. Although the force-type interaction is mainly discussed, the moment-type interaction is also introduced. Formulation of the DEM contact taking into account thermal effects as well as thermomechanical coupling finishes this review.

## 1 Introduction

The term discrete element method (DEM) comprises a family of numerical methods for analysis of discontinuous problems of mechanics of systems of particles (discrete elements) interacting with one another by contact. The DEM is a relatively new numerical method, it was introduced in the 70-s and 80-s of the 20th century in the pioneering works by Cundall (1971), Cundall and Strack (1979) and Walton (1982, 1983). The DEM was further developed in the works of Williams et al. (1985), Bardet and Proubet (1991), Moreau (1994) and many others. It has become a powerful tool for predicting the behaviour of various particulate and non-particulate materials

J. Rojek (✉)
Institute of Fundamental Technological Research,
Polish Academy of Sciences, Warsaw, Poland
e-mail: jrojek@ippt.pan.pl



A. Popp and P. Wriggers (eds.), *Contact Modeling for Solids and Particles*,
CISM International Centre for Mechanical Sciences 585,
https://doi.org/10.1007/978-3-319-90155-8_4

which can be represented by systems of particles, such as soils (Widuliński et al. 2009), powders (Martin et al. 2003), rocks (Cundall 1987; Potyondy and Cundall 2004; Rojek et al. 2011; Zubelewicz and Mroz 1983), concrete (Hentz et al. 2004; Wu et al. 2013), ceramics (Senapati and Zhang 2010) and even metals (Fleissner et al. 2007).

Discrete elements can be of an arbitrary shape (Rothenburg and Bathurst 1992; Tao et al. 2014; Cundall 1988), however, spherical particles are often a preferable choice (Cundall 1987; Widuliński et al. 2009; Plassiard et al. 2009) because of the simplicity of the formulation and the computational efficiency of contact detection algorithms for spherical objects. The present review will deal with the discrete element formulation employing spherical particles.

The contact algorithm plays an essential role in the discrete element method. The contact forces control the motion of the discrete elements and govern the macroscopic behaviour of the particle assembly. Two different approaches to contact treatment in the DEM can be identified, the so-called *soft-contact* approach (Cundall and Strack 1979; Cundall 1987; Potyondy and Cundall 2004) and the *hard-contact* concept (Hong and McLennan 1992; Haff and Werner 1987; Richardson et al. 2011). The soft-contact approach employs regularization of the contact constraints, while the hard-contact approach uses the methods of nonsmooth analysis to solve the problem with unilateral contact constraints.

In the soft-contact DEM formulation, a small overlap of the particles is allowed – the contact non-penetration conditions are satisfied approximately, only. The contact between the particles is assumed to last much longer than the time step, and the contact force evolution is analysed.

In the hard-contact approach, particle penetration is not allowed. The change of the particle momentum due to a collision is determined. The collision time is assumed to be very short and therefore it can be neglected. The contact force variation is not analysed.

In the present work, the soft-contact approach is considered. This approach allows us to adopt a suitable contact model for single particle collisions as well as an adequate model to obtain a required macroscopic behaviour. The present chapter is aimed to present basic concepts of contact modelling in the discrete element method.

The outline of the present chapter is as follows. The formulation of the discrete element method is presented in Sect. 2. Basic assumptions, equations of motion and time integration scheme are briefly described. Section 3 is devoted to contact modelling. Contact conditions are formulated, the penalty regularization of the contact constraints is introduced. Elementary contact mechanisms included in contact models are presented. Selected more complex contact models for force-type interaction are reviewed in Sect. 4. Their formulation and performance in simple problems are presented. The moment-type interaction is introduced in Sect. 5. An extension of the discrete element method on thermal and thermomechanical problems is presented in Sect. 6. Formulation of the thermal and thermomechanical contact is briefly discussed.

# 2 Discrete Element Method Formulation

## 2.1 Basic Assumptions

Dynamics of a system of interacting rigid cylindrical (in 2D) or spherical (in 3D) particles will be considered. Both translational and rotational motion of the particles will be taken into account. Initial positions and velocities (both linear and angular ones) of the particles are assumed to be known. The particles are subjected to an external load including point forces and moments, gravity and background damping (due to the interaction of particles with surrounding medium). The particles are assumed to interact by contact with one another and with other obstacles.

The problem to be solved is formulated as an initial-value problem defined by the ordinary differential equations (equations of motion) and appropriate initial conditions supplemented with contact constraints.

## 2.2 Equations of Motion

The motion of discrete elements (particles) is governed by the standard Newton–Euler equations of rigid body dynamics. The translational and rotational motion of the centre of mass of the $i$-th spherical or cylindrical element (Fig. 1) is described by the following equations:

$$m_i \ddot{\boldsymbol{u}}_i = \boldsymbol{F}_i \,, \tag{1}$$

$$J_i \dot{\boldsymbol{\omega}}_i = \boldsymbol{T}_i \,, \tag{2}$$

where $\boldsymbol{u}_i$ is the element centroid displacement in a fixed (inertial) coordinate frame $\boldsymbol{X}$:

$$\boldsymbol{u}_i = \boldsymbol{x}_i - \boldsymbol{X}_i \,, \tag{3}$$

$\boldsymbol{\omega}_i$ – the angular velocity, $\boldsymbol{F}_i$ – the resultant force, $\boldsymbol{T}_i$ – the resultant moment about the central axes, $m_i$ – the element mass, and $J_i$ is the moment of inertia which is

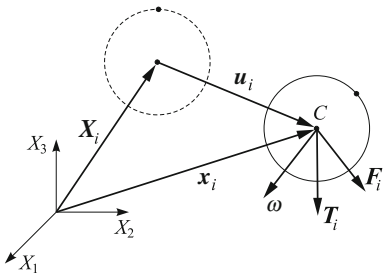


**Fig. 1** Motion of a discrete element

given by:

$$J_i = \frac{1}{2} m_i R_i^2 \quad \text{for a cylinder,} \tag{4}$$

$$J_i = \frac{2}{5} m_i R_i^2 \quad \text{for a sphere,} \tag{5}$$

$R_i$ being the $i$-th particle radius. The form of the rotational Eq. (2) is valid for spheres and cylinders (in 2D) and it is simplified with respect to a general form for an arbitrary rigid body with the rotational inertial properties represented by a second order tensor. The vectors $\boldsymbol{F}_i$ and $\boldsymbol{T}_i$ are sums of:

(i) all forces and moments applied to the $i$-th element due to an external load, $\boldsymbol{F}_i^{\text{ext}}$ and $\boldsymbol{T}_i^{\text{ext}}$, respectively,
(ii) force- and moment-type contact interactions with neighbouring spheres and all other obstacles, $\boldsymbol{F}_{ij}^{\text{cont}}$ and $\boldsymbol{T}_{ij}^{\text{cont}}$, respectively, $j = 1, \ldots, n_i^{\text{c}}$, where $n_i^{\text{c}}$ are the number of elements being in contact with the $i$-th discrete element,
(iii) forces and moments resulting from external (background) damping, $\boldsymbol{F}_i^{\text{damp}}$ and $\boldsymbol{T}_i^{\text{damp}}$, respectively.

Thus, the vectors $\boldsymbol{F}_i$ and $\boldsymbol{T}_i$ can be written as follows:

$$\boldsymbol{F}_i = \boldsymbol{F}_i^{\text{ext}} + \sum_{j=1}^{n_i^{\text{c}}} \boldsymbol{F}_{ij}^{\text{cont}} + \boldsymbol{F}_i^{\text{damp}}, \tag{6}$$

$$\boldsymbol{T}_i = \boldsymbol{T}_i^{\text{ext}} + \sum_{j=1}^{n_i^{\text{c}}} \boldsymbol{s}_{ij}^{\text{c}} \times \boldsymbol{F}_{ij}^{\text{cont}} + \sum_{j=1}^{n_i^{\text{c}}} \boldsymbol{T}_{ij}^{\text{cont}} + \boldsymbol{T}_i^{\text{damp}}, \tag{7}$$

where $\boldsymbol{s}_{ij}^{\text{c}}$ is the vector connecting the centre of mass of the $i$-th element with the contact point with the $j$-th element (Fig. 2).

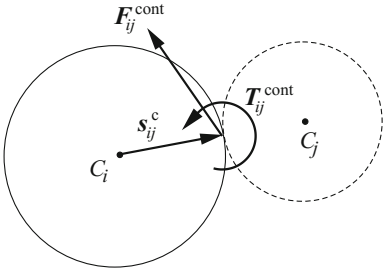


**Fig. 2** Contact interaction between two discrete elements

## 2.3 Time Integration Scheme

Equations of motion (1) and (2) are integrated in time using the explicit central difference scheme. The time integration operator for the translational motion at the $n$-th time step is as follows:

$$\ddot{\boldsymbol{u}}_i^n = \frac{\boldsymbol{F}_i{}^n}{m_i}\,, \tag{8}$$

$$\dot{\boldsymbol{u}}_i^{n+1/2} = \dot{\boldsymbol{u}}_i^{n-1/2} + \ddot{\boldsymbol{u}}_i^n \Delta t\,, \tag{9}$$

$$\boldsymbol{u}_i^{n+1} = \boldsymbol{u}_i^n + \dot{\boldsymbol{u}}_i^{n+1/2} \Delta t\,. \tag{10}$$

The first two steps in the integration scheme for the rotational motion are identical to those given by Eqs. (8) and (9):

$$\dot{\boldsymbol{\omega}}_i^n = \frac{\boldsymbol{T}_i{}^n}{\boldsymbol{J}_i}\,, \tag{11}$$

$$\boldsymbol{\omega}_i^{n+1/2} = \boldsymbol{\omega}_i^{n-1/2} + \dot{\boldsymbol{\omega}}_i^n \Delta t\,. \tag{12}$$

The vector of incremental rotations $\Delta\boldsymbol{\theta}_i$ is calculated as

$$\Delta\boldsymbol{\theta}_i = \boldsymbol{\omega}_i^{n+1/2} \Delta t\,, \tag{13}$$

Knowledge of the incremental rotation suffices to update the tangential contact forces. If necessary it is also possible to track the total change of rotational position of particles (Argyris 1982). Then, the rotation matrices between the moving frames embedded in the particles and the fixed global frame must be updated incrementally using an adequate multiplicative scheme (Rojek et al. 2001).

Explicit integration in time yields high computational efficiency of the solution for a single step. The disadvantage of the explicit integration scheme is its conditional numerical stability imposing the limitation on the time step $\Delta t$. The time step $\Delta t$ must not be larger than a critical time step $\Delta t_{\mathrm{cr}}$

$$\Delta t \leq \Delta t_{\mathrm{cr}} \tag{14}$$

determined by the highest natural frequency of the system $\nu_{\max}$

$$\Delta t_{\mathrm{cr}} = \frac{2}{\nu_{\max}}\,. \tag{15}$$

Exact determination of the highest frequency $\nu_{\max}$ would require solution of the eigenvalue problem defined for the whole system of connected rigid particles. The maximum frequency of the whole system can be estimated as the maximum of

natural frequencies $\nu_i^e$ of subsets of connected particles surrounding each particle $e$, cf. Belytschko et al. (1985):

$$\nu_{\max} \leq \nu_{\max}^D, \quad \text{where} \quad \nu_{\max}^D = \max_{i,e} \nu_i^e \tag{16}$$

## 3 Contact Modelling

### 3.1 Contact Conditions

The contacting pairs of discrete elements are identified by different search procedures. The contacting particles should satisfy contact constraints. The contact constraints can be expressed in terms of contact interactions and appropriate kinematic parameters.

It is assumed that the contact is concentrated at a point called the contact point and the contact interaction between two particles $i$ and $j$ consists of a concentrated force $\boldsymbol{F}_{ij}^{\text{cont}}$ and a concentrated moment $\boldsymbol{T}_{ij}^{\text{cont}}$ applied at the contact point (Fig. 2). The moment-type resistance will be discussed later on, here, the force interaction will be examined.

The contact force $\boldsymbol{F}_{ij}^{\text{cont}}$ can be decomposed into the normal and tangential components, $(\boldsymbol{F}_{\text{n}}^{\text{cont}})_{ij}$ and $(\boldsymbol{F}_{\text{t}}^{\text{cont}})_{ij}$, respectively

$$\boldsymbol{F}_{ij}^{\text{cont}} = (\boldsymbol{F}_{\text{n}}^{\text{cont}})_{ij} + (\boldsymbol{F}_{\text{t}}^{\text{cont}})_{ij} = (F_{\text{n}}^{\text{cont}})_{ij}\boldsymbol{n}_{ij} + (\boldsymbol{F}_{\text{t}}^{\text{cont}})_{ij}, \tag{17}$$

where $\boldsymbol{n}_{ij}$ is the unit vector normal at the contact point defined as follows

$$\boldsymbol{n}_{ij} = \frac{\boldsymbol{x}_j - \boldsymbol{x}_i}{\|\boldsymbol{x}_j - \boldsymbol{x}_i\|} \tag{18}$$

It is assumed that the normal and tangential contact can be decoupled and can be considered separately. The Signorini conditions for the unilateral (without adhesion) contact in the normal direction can be written as follows[1]:

$$F_{\text{n}}^{\text{cont}} \leq 0, \quad g \geq 0, \quad F_{\text{n}}^{\text{cont}} g = 0, \tag{19}$$

where $g$ is the gap between the particles (see Fig. 3):

$$g = d_{ij} - R_i - R_j \tag{20}$$

$d_{ij}$ being the distance between the particle centres

[1] In the next part of this section indices denoting the elements will be omitted.

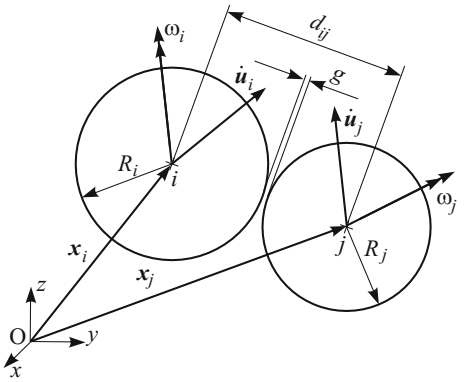


**Fig. 3** Definition of geometrical and kinematical parameters in the contact of two particles

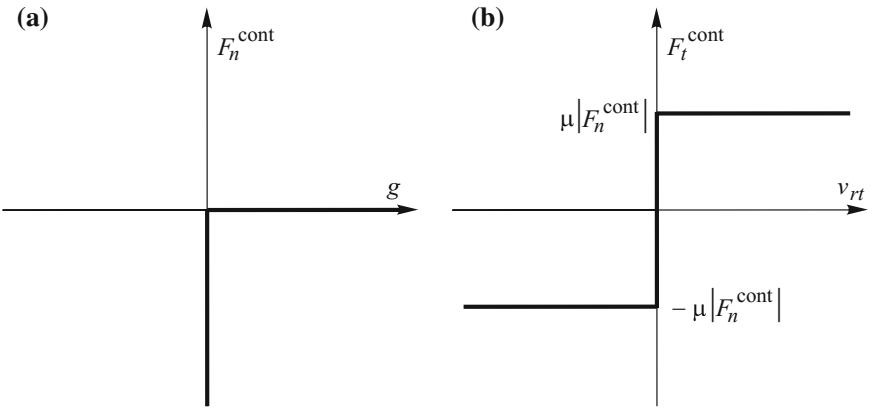


**Fig. 4** Graphs of contact laws: **a** unilateral normal contact, **b** tangential Coulomb friction contact

$$d_{ij} = \|\boldsymbol{x}_j - \boldsymbol{x}_i\| \tag{21}$$

The first inequality in Eq. (19) expresses the intensility condition (no tensile force is allowed), the second one specifies the impenetrability condition, and the third condition, called the complementarity condition, enforces the alternative, either $F_{\text{n}}^{\text{cont}} < 0$ and $g = 0$ or $F_{\text{n}}^{\text{cont}} = 0$ and $g > 0$. The unilateral normal contact law is illustrated graphically in Fig. 4a. In the adhesive (bilateral) contact, the tensile contact force is allowed, and the geometric inequality constraint $(19)_2$ is replaced by the equality constraint $g = 0$ (Curnier 1999). A rigorous mathematical treatment of the bilateral contact is much more complicated than that of the unilateral contact.

The tangential interaction is typically caused by interparticle friction. The complementary conditions for the frictional sliding contact in the tangential direction can be written as follows, cf. Klarbring (1999):

$$\phi_t \leq 0\,, \quad \lambda_t \geq 0\,, \quad \phi_t \lambda_t = 0\,, \tag{22}$$

where $\phi_t$ is the slip criterion and the non-negative parameter $\lambda_t$ is defined by the slip law:

$$\boldsymbol{v}_{\mathrm{rt}} = \lambda_t \frac{\boldsymbol{F}_{\mathrm{t}}^{\mathrm{cont}}}{\|\boldsymbol{F}_{\mathrm{t}}^{\mathrm{cont}}\|}\,. \tag{23}$$

where $\boldsymbol{v}_{\mathrm{rt}}$ is the relative tangential velocity at the contact point:

$$\boldsymbol{v}_{\mathrm{rt}} = \boldsymbol{v}_{\mathrm{r}} - v_{\mathrm{rn}} \boldsymbol{n}_{ij}\,. \tag{24}$$

with $\boldsymbol{v}_{\mathrm{r}}$ and $v_{\mathrm{rn}}$ being the total and normal relative velocities at the contact point given by

$$\boldsymbol{v}_{\mathrm{r}} = (\dot{\boldsymbol{u}}_j + \boldsymbol{\omega}_j \times \boldsymbol{s}_{ji}^c) - (\dot{\boldsymbol{u}}_i + \boldsymbol{\omega}_i \times \boldsymbol{s}_{ij}^c)\,, \tag{25}$$

$$v_{\mathrm{rn}} = \boldsymbol{v}_{\mathrm{r}} \cdot \boldsymbol{n}_{ij}\,, \tag{26}$$

where $\dot{\boldsymbol{u}}_i$ and $\dot{\boldsymbol{u}}_j$ are the translational velocities of the particle mass centres, $\boldsymbol{\omega}_i$ and $\boldsymbol{\omega}_j$ – the angular particle velocities, and $\boldsymbol{s}_{ij}^c$ are $\boldsymbol{s}_{ji}^c$ – the vectors connecting the particle mass centres to the contact points.

There are various models for the threshold of sliding, cf. Raous (1999). The most commonly used model is the Coulomb friction model, for which the slip criterion is given by:

$$\phi_t = \|\boldsymbol{F}_{\mathrm{t}}^{\mathrm{cont}}\| - \mu |F_{\mathrm{n}}^{\mathrm{cont}}| \leq 0 \tag{27}$$

where $\mu$ is the Coulomb friction coefficient. The graph corresponding to the Coulomb friction contact is given in Fig. 4b. The Coulomb friction coefficient is usually assumed constant, however, it can also be taken as a variable, for instance, dependent on the sliding velocity.

## 3.2 Regularization of the Contact Conditions

The discrete element method based on the soft contact approach imposes a penalty-type regularization of the unilateral (normal) and frictional contact constraints. The penalty regularization of the normal contact conditions is accomplished by taking

$$F_{\mathrm{n}}^{\mathrm{cont}} = k_n g\,, \quad \text{if} \quad g < 0\,, \tag{28}$$

where $k_n$ is a certain penalty parameter. The contact conditions $(19)_1$ and $(19)_3$ are still valid. The impenetrability condition $(19)_2$ is satisfied approximately, only. A certain overlap between the contacting particles

$$h = -g > 0 \tag{29}$$

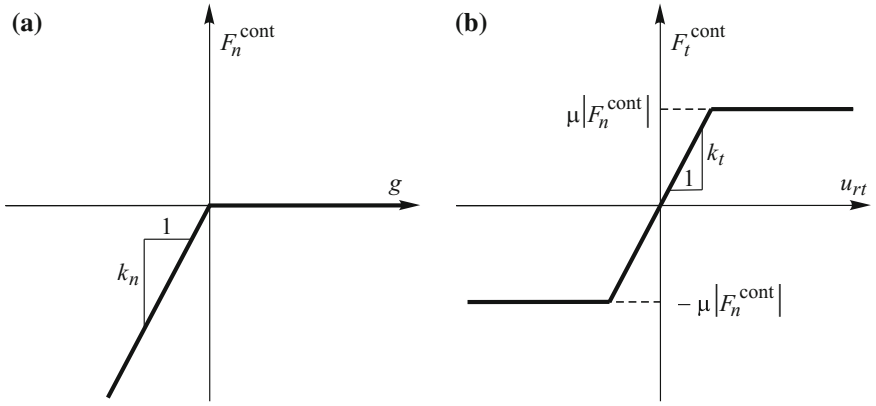


**Fig. 5** Graphs of regularized contact laws: **a** normal contact, **b** tangential Coulomb friction contact

is allowed. The penalization is exact if $k_n \to \infty$. We should remember, however, that large penalty values lead to small critical time steps given by Eq. (15). The penalization of the normal contact is illustrated graphically in Fig. 5a.

The regularization of the frictional constraints is carried out by introducing into Eq. (23) a tangential penalty $k_t$

$$\boldsymbol{v}_{\text{rt}} - \lambda_t \frac{\boldsymbol{F}_{\text{t}}^{\text{cont}}}{\|\boldsymbol{F}_{\text{t}}^{\text{cont}}\|} = \frac{\dot{\boldsymbol{F}}_{\text{t}}^{\text{cont}}}{k_t}\,, \tag{30}$$

Equation (30) shows that the penalty regularization of the Coulomb frictional constraints introduces a decomposition of the total slip velocity $\boldsymbol{v}_{\text{rt}}$ into the reversible and irreversible parts, $\boldsymbol{v}_{\text{rt}}^{\text{r}}$ and $\boldsymbol{v}_{\text{rt}}^{\text{ir}}$, respectively:

$$\boldsymbol{v}_{\text{rt}} = \boldsymbol{v}_{\text{rt}}^{\text{r}} + \boldsymbol{v}_{\text{rt}}^{\text{ir}}\,, \tag{31}$$

where

$$\boldsymbol{v}_{\text{rt}}^{\text{r}} = \frac{\dot{\boldsymbol{F}}_{\text{t}}^{\text{cont}}}{k_t}\,, \tag{32}$$

$$\boldsymbol{v}_{\text{rt}}^{\text{ir}} = \lambda_t \frac{\boldsymbol{F}_{\text{t}}^{\text{cont}}}{\|\boldsymbol{F}_{\text{t}}^{\text{cont}}\|}\,. \tag{33}$$

The graph corresponding to the regularized Coulomb friction model is shown in Fig. 5b, where the tangential contact force $F_{\text{t}}^{\text{cont}}$ has been plotted as a function of the relative tangential displacement evaluated by integrating the relative tangential velocity

$$u_{\text{rt}} = \int v_{\text{rt}}\, \mathrm{d}t\,. \tag{34}$$

### 3.3 Physical Interpretation of the Penalty Regularization

Penalization of the normal and tangential contact constraints is equivalent to specifying additional constitutive relations on the interface. Thus, the elastic behaviour has been introduced above for compression in the normal contact, and the frictional contact has been reformulated as a problem analogous to that of elastoplasticity.

The overlap of the contacting particles $h$ defined by Eq. (29) is assumed to represent an effect of a local deformation of the particles at the contact point due to the contact interaction (Fig. 6). This assumption gives a possibility to define different force–overlap relationships in order to represent better various deformation mechanisms at the contact zone. Similarly, different force–slip relationships can be defined for the tangential contact.

It must be remarked that it is assumed that the particle deformation due to contact is localized and it does not affect other particle contacts. This assumption is justified if the deformation of real particles is relatively small.

### 3.4 Elementary Contact Deformation Mechanisms

Contact models may take into account different deformation mechanisms and physical phenomena involved in contact. Typical elementary contact deformation mechanisms and associated effects are summarized below.

*Elasticity*

The contact force in the normal or tangential direction is given by a linear or nonlinear function of a displacement-type variable $u$. A linear elastic model defines the force through the relation

$$F = ku\,, \tag{35}$$

where $k$ is a constant stiffness parameter, and the displacement-type variable $u$ can represent the particle overlap or the tangential relative displacement. A nonlinear

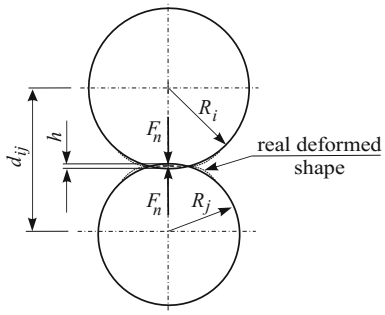


**Fig. 6** Overlap of the contacting particles

elastic model is characterized by a variable stiffness. The displacement in an elastic contact model is completely reversible.

*Plasticity*
A linear or nonlinear force–displacement relationship is obtained from the response of particles undergoing plastic deformation due to contact pressure. The displacement in an ideally plastic contact model is completely irreversible. The theory of plasticity provides a suitable framework for modelling the friction.

*Viscosity*
A contact force due to a viscous response at the contact interaction is defined by a force–velocity relationship:

$$F = \eta \dot{u} \,, \tag{36}$$

where $\eta$ represents viscous properties of the contact interface. It can be assumed constant in a linear viscous model or variable in a nonlinear model. A viscous model can be used to represent physical phenomena such as damping or creep.

*Friction*
Friction being a dissipation mechanism opposing the tangential relative motion of contacting particles is sometimes called dry damping, cf. Zonetti et al. (1999), as opposed to velocity dependent viscous damping mentioned above. The Coulomb model is the most popular model of friction. The graph presenting the contact force in the Coulomb model is presented in Fig. 4b.

*Cohesion/adhesion*
Modelling of cohesive materials such as rocks or concrete with discrete elements requires accounting for cohesion or adhesion in the contact model. Cohesive/adhesive bonds are introduced between contacting particles. These bonds transfer contact forces opposing the separation of particles in the normal direction as well as the relative motion in the tangential direction.

*Damage*
Damage represents deterioration of mechanical material properties such as stiffness and strength caused by the development of internal cracks. Accounting for damage effects in the contact allows us to consider a gradual deterioration of mechanical properties represented by cohesive bonds.

*Fracture*
Accumulated damage can lead to a complete deterioration of the cohesive bonds. The cohesive bonds can also be assumed to be broken in a brittle way when the strength of the cohesive bonds is exceeded. In this way initiation and development of fracture in the material can be modelled in the discrete element method.

*Thermal effects*
Contact with friction is accompanied by heat generation. The heat generated through friction is absorbed and conducted by the particles. An increasing temperature of contacting particles may affect mechanical contact properties such as the contact stiffness, viscosity or friction coefficient (Shillor et al. 2004). Formulation of the

contact model accounting for thermal effects as well as thermal and thermomechanical formulation of the discrete element method will be presented further on.

Contact models in the discrete element method usually incorporate different mechanisms and effects described above which allow us to model complex behaviour of real materials. Contact models similarly to constitutive material models are often represented graphically by rheological schemes. The rheological schemes are built from rheological elements representing elementary mechanisms. Typical rheological elements are shown in Fig. 7.

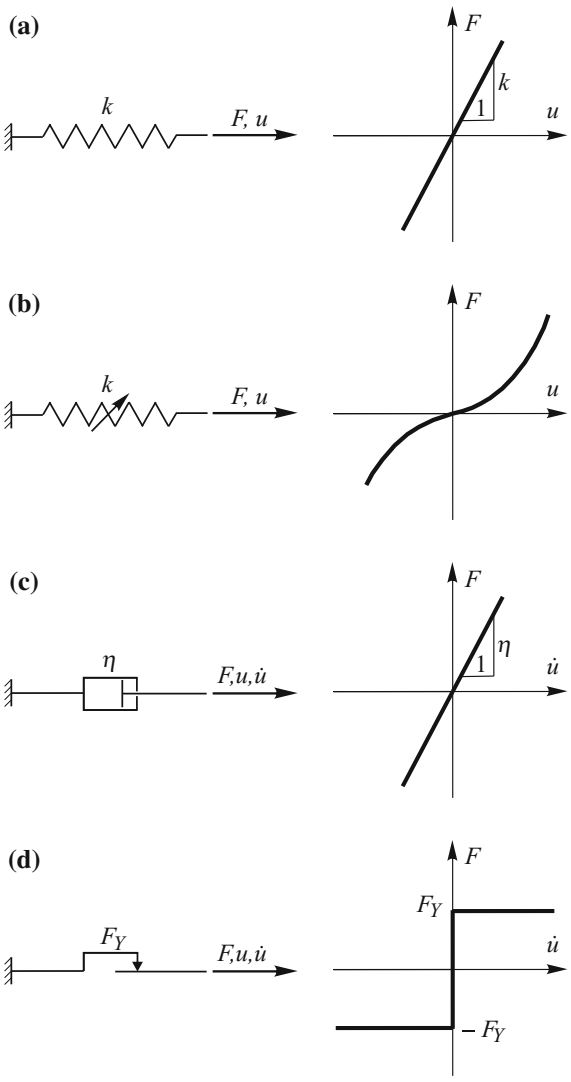


**Fig. 7** Rheological elements and plots of the corresponding constitutive relationships: **a** linear spring, **b** nonlinear spring, **c** linear dashpot, **d** slider

The linear and nonlinear springs (Fig. 7a, b) represent elastic properties in a rheological scheme, the linear dashpot (Fig. 7b) corresponds to the viscous effects described by Eq. (36), the slider (Fig. 7d) is used for the friction, the slider alone represents the non-regularized Coulomb friction model, when connected in series with a spring, it can represent the regularized Coulomb friction model.

# 4 Selected Contact Models

## *4.1 Linear Viscoelastic Contact Model with Coulomb Friction*

### Formulation of the model

The model presented here is similar to the model proposed in the pioneering work by Cundall and Strack (1979). The rheological scheme of the model is shown in Fig. 8. The normal contact force is represented by the viscoelastic Kelvin–Voigt element composed of a linear spring connected in parallel with a linear dashpot. The element corresponding to the tangential contact force is constituted by a spring in series with a slider.

The normal contact force $F_{\mathrm{n}}^{\mathrm{cont}}$ transmitted by the Kelvin–Voigt element is composed of the elastic part transferred by the spring $F_{\mathrm{n}}^{\mathrm{e}}$ and the viscous damping part transferred by the dashpot $F_{\mathrm{n}}^{\mathrm{d}}$:

$$F_{\mathrm{n}}^{\mathrm{cont}} = F_{\mathrm{n}}^{\mathrm{e}} + F_{\mathrm{n}}^{\mathrm{d}} \tag{37}$$

The elastic part is evaluated according to the linear relationship analogical to Eq. (28)

$$F_{\mathrm{n}}^{\mathrm{e}} = k_{\mathrm{n}} g \,, \tag{38}$$

where $k_{\mathrm{n}}$ is the normal contact stiffness and $g$ is defined by Eq. (20). The formula (38) is used for $g < 0$. A negative value of $g$ denotes a particle overlap. If $g \geq 0$ the elastic contact force is set to zero ($F_{\mathrm{n}}^{\mathrm{e}} = 0$).

The damping part is evaluated according to the linear relationship analogical to Eq. (36)

$$F_{\mathrm{n}}^{\mathrm{d}} = c_{\mathrm{n}} v_{\mathrm{rn}} \,, \tag{39}$$

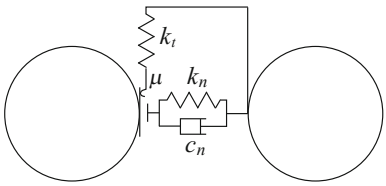


**Fig. 8** Rheological scheme of the viscoelastic contact model with the Coulomb friction

where $c_{\mathrm{n}}$ is the normal viscous damping parameter and $v_{\mathrm{rn}}$ is the normal relative velocity at the contact defined by Eq. (26).

The tangential part of the contact model presented graphically in Fig. 8 corresponds to the regularized Coulomb friction model described in Sect. 3.2. The stiffness of the linear spring $k_t$ corresponds to the penalty parameter introduced in Eq. (30). The slider is blocked until the slip criterion (27) is achieved. The graph of the tangential contact force versus relative tangential displacement is shown in Fig. 5.

The analogy of the regularized frictional contact model to the elastoplasticity commented above, allows us to calculate the friction force employing the radial return algorithm analogous to that used in elastoplasticity. First a trial state is calculated

$$\boldsymbol{F}_t^{\mathrm{trial}} = \boldsymbol{F}_t^{\mathrm{old}} - k_t \boldsymbol{v}_{rt} \Delta t \,, \tag{40}$$

and then the slip condition is checked

$$\phi^{\mathrm{trial}} = \|\boldsymbol{F}_t^{\mathrm{trial}}\| - \mu |F_n| \,. \tag{41}$$

If $\phi^{\mathrm{trial}} \leq 0$, we have the case of stick contact and the friction force is assigned the trial value

$$\boldsymbol{F}_t^{\mathrm{new}} = \boldsymbol{F}_t^{\mathrm{trial}} \,, \tag{42}$$

otherwise (slip contact) a return mapping is performed

$$\boldsymbol{F}_t^{\mathrm{new}} = \mu |F_n| \frac{\boldsymbol{F}_t^{\mathrm{trial}}}{\|\boldsymbol{F}_t^{\mathrm{trial}}\|} \,. \tag{43}$$

**Evaluation of the model parameters**

There are different approaches to evaluating the contact stiffness $k_n$ in the DEM. It can be taken as uniform in the whole discrete element assembly (Rojek et al. 2005) or it can be calculated locally, usually assuming that it depends on the contacting particle size (Potyondy and Cundall 2004) and it can be given by certain functions of the particle radii $R_i$ and $R_j$:

$$k_n = f_k(R_i, R_j) \,. \tag{44}$$

Different assumptions for the form of the functions $f_k(R_i, R_j)$ have been discussed by Rojek et al. (2012). Here, one of them will be presented.

The spring modelling contact elasticity can be treated as equivalent to an elastic bar of a non-uniform cross-sectional area (Fig. 9), consisting of two segments, with the lengths

$$L_i = R_i \,, \quad L_j = R_j \tag{45}$$

and the cross-sectional areas

$$A_i = \alpha_i \pi (R_i)^2 \,, \quad A_j = \alpha_j \pi (R_j)^2 \tag{46}$$

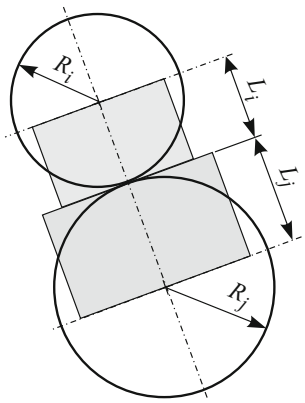


**Fig. 9** Schematic connection of two particles

where $0 \leq \alpha_i, \alpha_j \leq 1$ are the coefficients defining the areas of the segments as fractions of the particle cross-sectional area.

The system of the two bar segments can be treated as two springs connected in series. The axial force $F^e$ transferred by the whole system is equal to the forces in the segments $i$ and $j$, $F_i^e$ and $F_j^e$:

$$F^e = F_i^e = F_j^e \tag{47}$$

The overall axial deformation of the system, assumed as equal to the overlap $g$ ($g < 0$), can be decomposed to the deformations of both segments, $g_i$ and $g_j$

$$g = g_i + g_j \tag{48}$$

The force–displacement relationships for each bar can be written in the following form:

$$F_i^e = k_n^i g_i \tag{49}$$

$$F_j^e = k_n^j g_j \tag{50}$$

where and $k_n^i$ and $k_n^j$ are stiffnesses of the segments $i$ and $j$. Substituting Eqs. (38), (49) and (50) into Eq. (48) and taking into account Eq. (47) we obtain the following equation for the stiffness $k_n$:

$$\frac{1}{k_n} = \frac{1}{k_n^i} + \frac{1}{k_n^j} \tag{51}$$

which can be transformed to the form

$$k_n = \frac{k_n^i k_n^j}{k_n^i + k_n^j} \tag{52}$$

Expression (52) is identical to that used by Potyondy and Cundall (2004).

Using the assumptions (45) and (46) the stiffness of the segments $i$ and $j$ can be expressed as follows:

$$k_n^i = \frac{E_i A_i}{L_i} = \alpha_i \pi E_i R_i \tag{53}$$

$$k_n^j = \frac{E_j A_j}{L_j} = \alpha_j \pi E_j R_j \tag{54}$$

where $E_i$ and $E_j$ are Young's moduli of the materials of the segments (or of the particles) $i$ and $j$. Introducing the relationships (53) and (54) into the formula (52) and assuming $E_i = E_j = E$ and $\alpha_i = \alpha_j = \alpha$, we obtain the expression for the equivalent stiffness $K$ in the following form:

$$k_n = \alpha \pi E R^* \tag{55}$$

where $R^*$ is the effective radius defined in terms of the particle radii, $R_i$ and $R_j$

$$\frac{1}{R^*} = \frac{1}{R_i} + \frac{1}{R_j}. \tag{56}$$

For equal size particles ($R_i = R_j = R$), Eq. (55) takes the form:

$$k_n = \frac{1}{2} \alpha \pi E R \tag{57}$$

The value of the tangential stiffness parameter $k_t$ is, in principle, independent of the normal stiffness parameter, however, it is usually defined with respect to it assuming a certain ratio $\beta$ of the normal and tangential stiffness

$$\beta = \frac{k_t}{k_n} \tag{58}$$

The ratio $\beta$ is very important, since it has a large influence on the macroscopic behaviour reproduced by the DEM model. Equivalent macroscopic properties, such as the Young's modulus or the Poisson's ratio can be presented as functions of the ratio $k_t/k_n$, cf. Marczewska et al. (2016).

The damping coefficient $c_\mathrm{n}$ can be related to the critical damping $C_\mathrm{cr}$ of the considered system:

$$\zeta = \frac{c_\mathrm{n}}{C_\mathrm{cr}} \tag{59}$$

where $\zeta$ is called the damping ratio. It is a non-negative dimensionless parameter ($\zeta \geq 0$). Zero damping ratio, $\zeta = 0$, indicates no damping, $0 < \zeta < 1$ – underdamping, $\zeta = 1$ – critical damping, and $\zeta > 1$ – overdamping. The critical damping $C_\mathrm{cr}$ for the system of two rigid bodies with masses $m_i$ and $m_j$, connected with a spring of the stiffness $k_n$, cf. Taylor and Preece (1992)

$$C_{\mathrm{cr}} = 2\sqrt{m^* k_{\mathrm{n}}}\,. \tag{60}$$

where the effective mass $m^*$ is defined by

$$\frac{1}{m^*} = \frac{1}{m_i} + \frac{1}{m_j}\,. \tag{61}$$

The damping ratio $\zeta$ can be expressed in terms of the coefficient of restitution (COR) $e$, cf. Nagurka and Huang (2006)

$$\zeta = -\frac{\ln e}{\sqrt{\pi^2 + (\ln e)^2}}\,. \tag{62}$$

The coefficient of restitution $e$ in the normal direction is defined as the ratio of moduli of the relative normal velocities after and before impact, $v_{\mathrm{rn}}^{\mathrm{end}}$ and $v_{\mathrm{rn}}^{0}$, respectively:

$$e = \frac{|v_{\mathrm{rn}}^{\mathrm{end}}|}{|v_{\mathrm{rn}}^{0}|}\,. \tag{63}$$

The relationship (62) is plotted in Fig. (10).

The viscous damping is used in the discrete element method as a mechanism allowing to dissipate energy in particle collisions, and achieve different response of the system to dynamic loading, including quasistatic response if an adequate damping is combined with a slowly applied loading. It must be remarked, however, that the viscous damping introduces certain inconsistencies in the contact model, which will be discussed in the first of numerical examples below.

**Numerical examples**

*Collision of two balls with given initial velocities*

The viscoelastic Kelvin–Voigt contact model is used to simulate a collision of two equal balls of radius $R = 10\,\mathrm{mm}$ moving along one line with equal but opposed

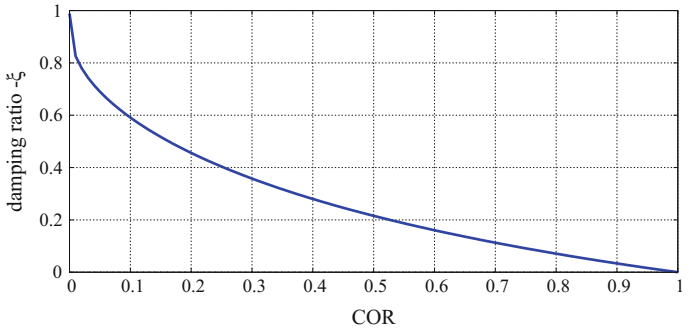


**Fig. 10** Relationship between the coefficient of restitution and the damping ratio

velocities $v = 10\,\text{m/s}$. The mass density $\rho = 8000\,\text{kg/m}^3$ has been assumed. The contact stiffness $k_n$ has been evaluated according to Eq. (57) taking the Young's modulus $E = 200\,\text{GPa}$, and the coefficient $\alpha = 0.04$. The effective contact stiffness $k_n = 1.26 \cdot 10^8\,\text{N/m}$ has been evaluated. Different values of damping characterized by coefficients of restitution (COR) $e = 0.1$, 0.5, 0.8 and 1 have been considered. The value $e = 1$ corresponds to an ideally elastic collision.

The gap between the balls and the velocity of one of the balls during the collision are plotted as functions of time in Fig. 11 for different damping. The duration of the collisions corresponds to the interval with negative values of the gap (see Fig. 11a. It can be seen Fig. 11b that after the collision the balls bounce off each other with the velocity dependent on the damping. In the elastic collision, the velocity of the ball after the collision is the same as before the collision. In the inelastic collisions, the velocity of the ball after the collision is lower than before the collision. The higher the damping is (or in other words, the lower the COR is), the lower the rebound velocity is.

Evolution of the total contact force and its components is plotted in Fig. 12 for different damping. The elastic, damping and total contact forces are given as functions of time in Figs. 12a, b and c, respectively. By comparing Figs. 11 and 12, it can be seen that the elastic force is proportional to the gap in agreement with Eq. (38), and

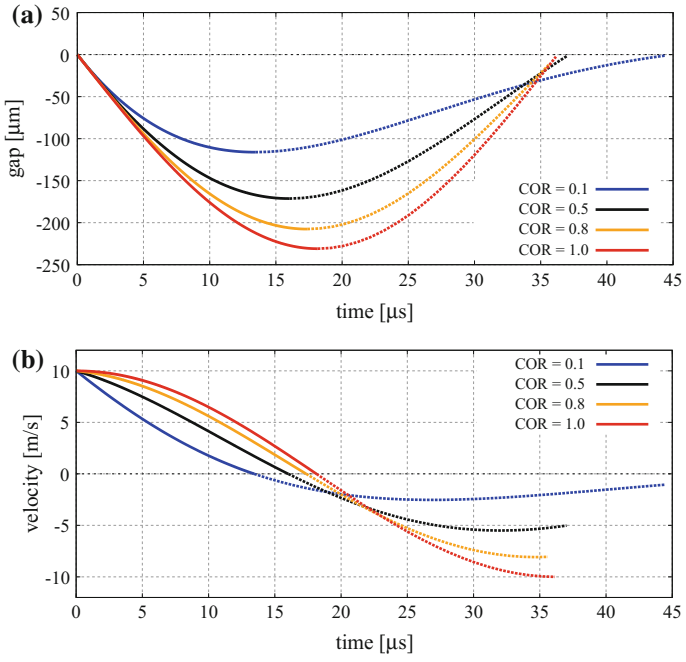


**Fig. 11** Evolution of contact kinematic parameters during collision of two balls in the linear Kelvin–Voigt model for different values of COR: **a** gap versus time, **b** velocity versus time (the solid parts of the curves represent loading and the broken ones – unloading)

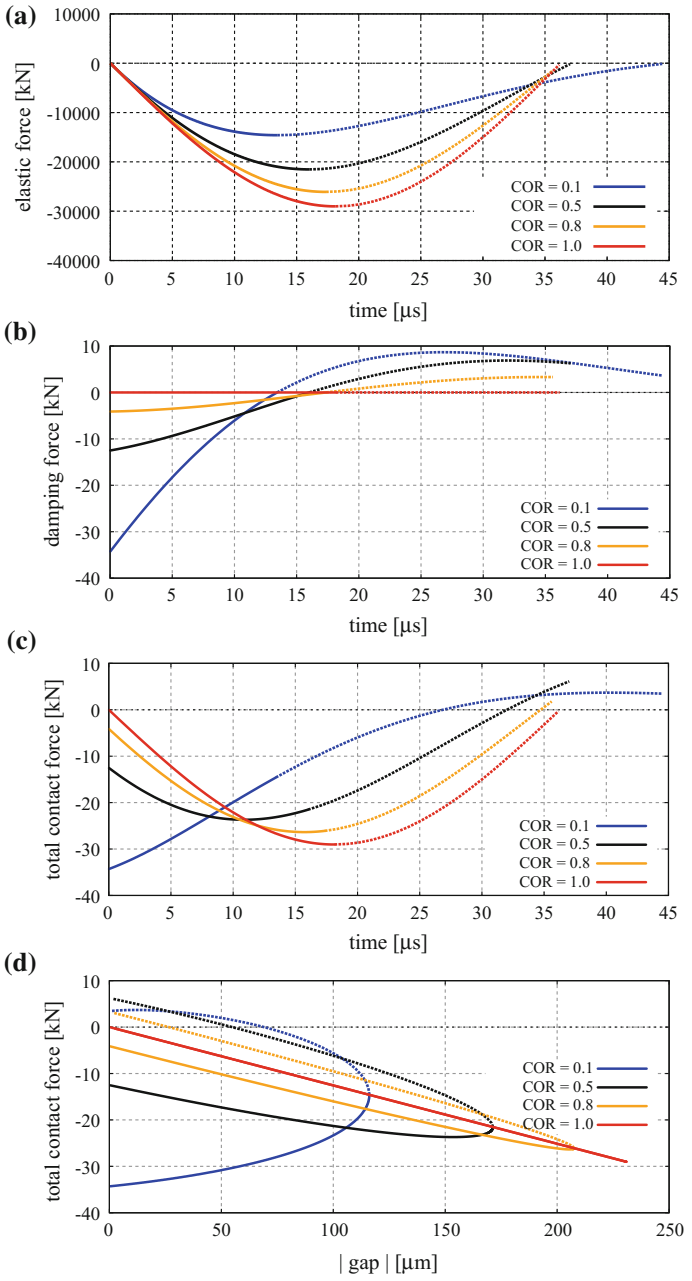


**Fig. 12** Evolution of contact forces during collision of two balls in the linear Kelvin–Voigt model for different values of COR (the solid parts of the curves represent loading and the broken ones – unloading)

the damping force is proportional to the velocity in agreement with Eq. (39). It can be observed in Fig. 12b that the damping force acquires a certain non-zero value at the beginning of the collision, and it has a non-zero value at the end of the collision. This, with the zero damping force before and after the collision, leads to discontinuity of the damping component during the analysed period of time. Due to the discontinuity of the viscous damping force, the total contact force $F_{\mathrm{n}}^{\mathrm{cont}}$ displayed in Fig. 12c is also discontinuous at the beginning and end of the collision while real contact forces are continuous.

Moreover, due to the viscous damping the total contact force $F_{\mathrm{n}}^{\mathrm{cont}}$ is cohesive in the final stage of the collision ($g < 0$ and $v_{\mathrm{rn}} > 0$), while the contact forces in cohesionless particle systems are always repulsive.

The inconsistencies of the linear viscoelastic contact model can be mitigated, at least partially, by replacing the linear spring and dashpot with appropriate nonlinear spring and damping elements as proposed by Hunt and Crossley (1975).

The curves of the total force versus gap for different damping are displayed in Fig. 12d. In the ideally elastic case (COR = 1), the loading and unloading force–gap relations coincide. In the damped collisions, the loading and unloading curves do not coincide and form a hysteresis loop. The area within the loop is a measure of energy lost during the collision (Lin and Hui 2002).

*Contact of two spheres under step loading*

A contact of two equal balls of radius $R = 10\,\mathrm{mm}$ subjected to step compressive loading $F = 20\,\mathrm{kN}$ has been analysed using the linear viscoelastic Kelvin–Voigt model. The same material properties as in the previous example have been assumed. The initial conditions are defined by the zero gap and zero ball velocities. Effect of the damping has been studied taking different values of coefficients of restitution COR = 0.05, 0.5, 0.8 and 1.

Figure 13 shows the time response of the systems in terms of the gap, velocity of one of the balls and total contact force. It can be seen that in the system with zero damping (COR = 1) the balls oscillate with the period which is in perfect agreement with the theoretical value

$$T = 2\pi\sqrt{\frac{m^*}{k_n}} = 72.6\ \mu\mathrm{s}\,.$$

The mean value of the gap (actually the overlap) oscillations coincides with the static state of equilibrium under the applied force

$$g = \frac{F_n}{k_n} = -159.1\ \mu\mathrm{m}\,.$$

The oscillations of the systems with damping are attenuated and the quasistatic state of equilibrium is achieved with the gap calculated above.

This shows a possibility to use the dynamic formulation to solve static problems which is a basic principle of the dynamic relaxation method, employed both in the

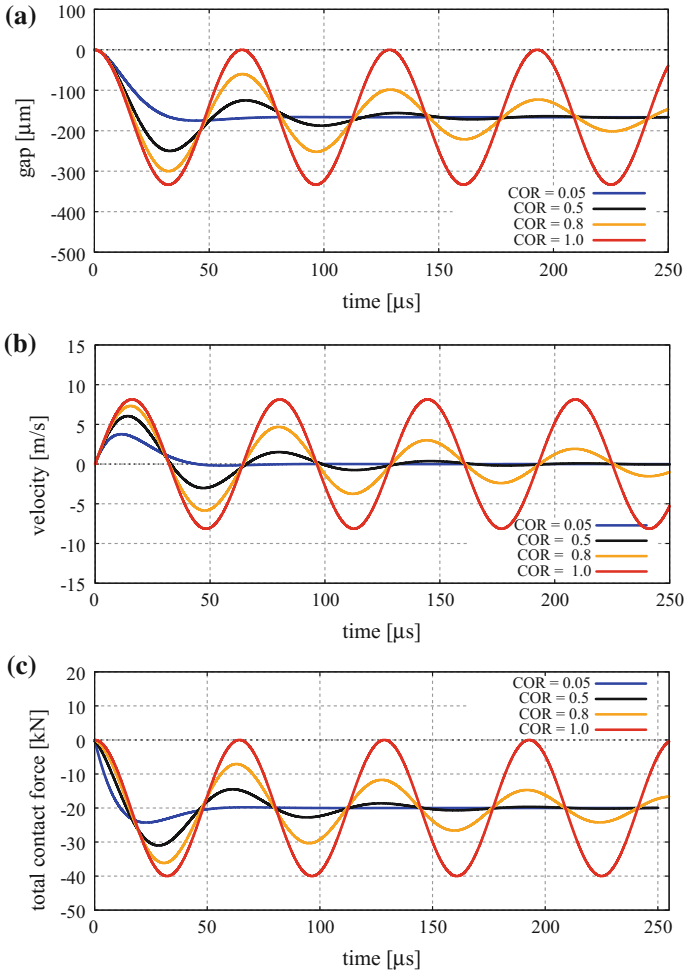


**Fig. 13** Evolution of contact kinematic variables and contact forces during contact of two spheres under step loading for different values of COR

discrete element method (Rojek et al. 2013) and the finite element method (Joldes et al. 2011). In the elastic linear problems solved by the dynamic relaxation method, the solution in the transient period is not important, and different values of damping allow us to arrive at the same static solution. The dynamic relaxation method can also be applied with certain cautiousness to path dependent problems.

*Contact of two spheres under linearly increasing loading*

The system of two balls, the same as in the previous example and with the same initial conditions, has been subjected to a compressive loading increasing linearly from 0 to 20 kN in the time interval from 0 to 0.5 s. Then, for $t > 0.5$ s the loading

has been kept constant. The contact of the balls has been analysed using the linear viscoelastic Kelvin–Voigt model with different values of damping defined by the coefficients of restitution COR = 0.1, 0.5 and 1.

Figure 14 shows the time response of the systems with different damping in terms of the gap, velocity of one of the balls and total contact force. The solution with zero damping (COR = 1) is characterized with oscillations. The oscillations are attenuated in the solutions with damping. For a sufficiently high level of the damping (low values of COR), the response in terms of the gap and contact force is practically linear, in agreement with the linear increase of the applied force. A

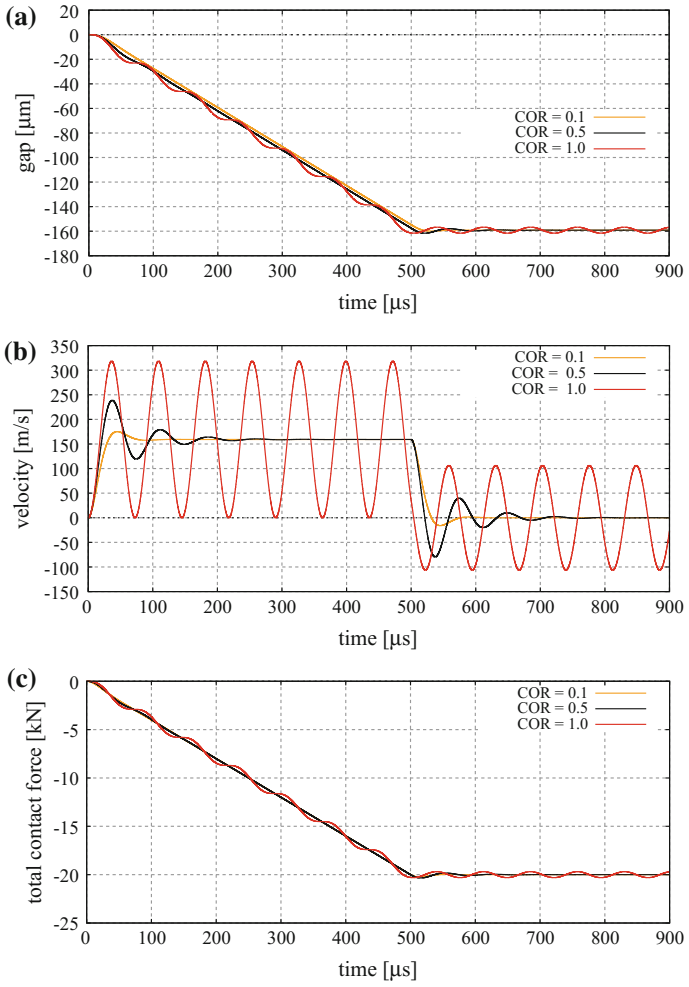


**Fig. 14** Evolution of contact kinematic variables and contact forces during contact of two spheres under linearly increasing loading for different values of COR

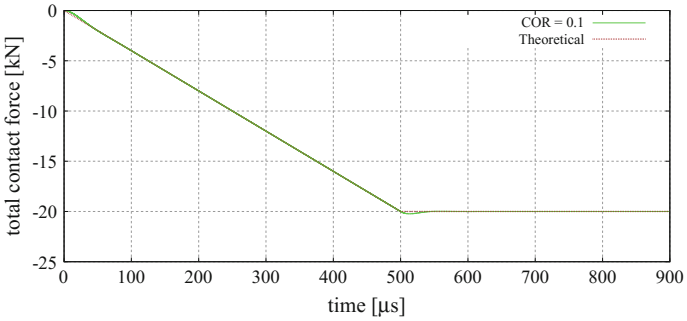


**Fig. 15** Comaprison of the numerical and theoretical contact force during contact of two spheres under linearly increasing loading

perfect agreement of the contact force with the applied force can be observed in Fig. 14, which confirms that the loading and response can be considered quasistatic. This demonstrates a possibility to reproduce quasistatic conditions in an incremental form (cf. also Fig. 15), which is important for the analysis of nonlinear and path dependent problems.

## *4.2 Viscoelastic Hertz–Mindlin–Deresiewicz Model*

### Formulation of the model

This model combines the Hertz-type viscoelastic model for the normal interaction with the Mindlin–Deresiewicz model of friction acting in the tangential direction. The rheological scheme of the model is similar to that shown in Fig. 8, the difference consisting in replacing the linear springs with nonlinear ones.

The Hertz model employs a nonlinear relationship for the evaluation of the elastic contact force based on the analytical solution of the contact problem between elastic spheres (Hertz 1882; Johnson 1985):

$$F_{\mathrm{n}}^{\mathrm{e}} = -K_{nHz} h^{\frac{3}{2}}, \tag{64}$$

where $h$ ($h = -g$) is the amount the particles' overlap and the contact stiffness parameter $K_{nHz}$ is given by the following formula:

$$K_{nHz} = \frac{4}{3} E^* \sqrt{R^*}, \tag{65}$$

where $E^*$ is the effective modulus of elasticity defined in terms of the Young's moduli, $E_i$ and $E_j$, and the Poisson's ratios, $\nu_i$ and $\nu_j$, of the two contacting particles

$$\frac{1}{E^*} = \frac{1-\nu_i^2}{E_i} + \frac{1-\nu_j^2}{E_j}\,, \tag{66}$$

and $R^*$ is the effective radius defined by Eq. (56). Please note that the contact force has been defined in Eq. (64) in terms of the overlap $h$ instead of the gap $g$ and the minus sign has been introduced in order to keep consistency with the earlier used sign convention treating the compressive contact forces as negative.

In the framework of the DEM, a viscous damping is commonly added to the elastic Hertz force in order to dissipate energy at particle collisions. A linear damping given by Eq. (39) is sometimes taken, cf. Lee (1994). More advanced models, however, use nonlinear damping terms in connection with the Hertzian elastic contact. Hunt and Crossley (1975) have derived the following general form of nonlinear damping

$$F_{\mathrm{n}}^{\mathrm{d}} = \eta_{\mathrm{n}} h^p v_{\mathrm{rn}}^q\,. \tag{67}$$

Tsuji et al. (1992) have proposed the damping term as above with $p = 1/4$ and $q = 1$:

$$F_{\mathrm{n}}^{\mathrm{d}} = \eta_{\mathrm{n}} h^{\frac{1}{4}} v_{\mathrm{rn}}\,. \tag{68}$$

The damping dissipation coefficient $\eta_{\mathrm{n}}$ used in Eq. (68) can be related to the nonlinear spring stiffness $K_{nHz}$ and the coefficient of restitution $e$ as follows (Navarro and de Souza Braun 2013):

$$\eta_{\mathrm{n}} = \sqrt{5}\sqrt{m^* K_{nHz}}\frac{\ln e}{\sqrt{\pi^2 + (\ln e)^2}}\,. \tag{69}$$

Different analytical relationships between the damping ratio and coefficient of restitution in the nonlinear viscoelastic contact model have been derived by (Jankowski 2006). Possibilities of improvements of viscous damping for the Hertz elastic contact are still investigated (Zdancevičius et al. 2017).

The Hertzian normal contact model is commonly combined with the tangential contact model according to Mindlin and Deresiewicz (1953). A full implementation of the Mindlin–Deresiewicz theory leads to complex algorithms, cf. (Renzo and Maio 2004; Kruggel-Emden et al. 2008), therefore different simplifications have been proposed. Employing the Mindlin and Deresiewicz solution for the constant normal force Tsuji et al. (1992) derived the formula for the tangential force:

$$F_t = k_t u_{rt}\,, \tag{70}$$

where the tangential stiffness $k_t$ is calculated as follows:

$$k_t = 8G^*\sqrt{R^* h}\,, \tag{71}$$

the effective shear modulus is defined in terms of the particles shear moduli, $G_i$ and $G_j$, and the Poisson's ratios, $\nu_i$ and $\nu_j$, by the following relationship

$$\frac{1}{G^*} = \frac{2-\nu_i}{G_i} + \frac{2-\nu_j}{G_j}\,, \tag{72}$$

the effective radius $R^*$ is defined by Eq. (56), $h$ is the particle overlap and the relative tangential displacement at the contact point $u_{rt}$ is obtained by integration of the relative tangential velocity:

$$u_{rt} = \int_0^t \boldsymbol{v}_{rt}\,\mathrm{d}t\,. \tag{73}$$

The tangential force $F_t$ is limited by the Coulomb condition

$$F_t \le \mu |F_n|\,. \tag{74}$$

In order to improve an agreement with the full Mindlin–Deresiewicz theory Renzo and Maio (2004); Maio and Renzo (2005) proposed a correction to the model developed by Tsuji et al. (1992) consisting in scaling the stiffness given by Eq. (71) by the factor 2/3.

$$k_t = \frac{2}{3}\left(8G^*\sqrt{R^*h}\right)\,, \tag{75}$$

**Numerical example**

*Collision of two balls with given initial velocities*

The viscoelastic Kelvin–Voigt contact model with the nonlinear Hertzian elastic component and the damping component evaluated according to Eqs. (68) and (69) has been used to simulate a collision of two equal balls analysed previously with the linear Kelvin–Voigt contact model. The same ball size (radius $R = 10\,\mathrm{mm}$), properties (mass density $\rho = 8000\,\mathrm{kg/m^3}$, Young's modulus $E = 200\,\mathrm{GPa}$) and initial conditions (velocities $v = 10\,\mathrm{m/s}$) as previously have been assumed. The set of data has been completed with the Poisson's ratio $\nu = 0.3$. Similarly as previously, different values of damping characterized by coefficients of restitution COR = 0.1, 0.5, 0.8 and 1 have been considered.

The evolution of the gap between the balls and the velocity of one of the balls for different damping have been plotted in Fig. 16a and b, respectively. It can be seen that the lower the COR is, the longer the impact and the lower the rebound velocity are.

The elastic, damping and total contact forces are plotted as functions of time in Fig. 17a, b and c, respectively. It can be observed in Fig. 17b that the damping contact force in the present model is no longer discontinuous on the contrary to the damping

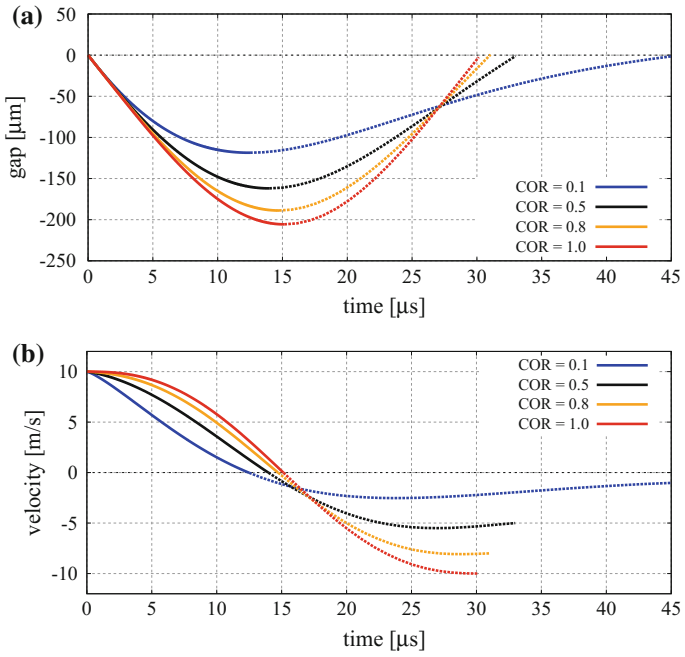


**Fig. 16** Evolution of contact kinematic parameters during collision of two balls in the nonlinear Kelvin–Voigt model for different values of COR (the solid parts of the curves represent loading and the broken ones – unloading)

force in the linear Kelvin–Voigt contact model displayed in Fig. 12b. Therefore, the total contact force in Fig. 17c is not discontinuous, either. The other imperfection of the linear Kelvin-Voigt model, manifested in cohesive interaction in the final stage of impact is not eliminated in the nonlinear Kelvin-Voigt model presented here, which can be noticed in Fig. 17c and d. Figure 12d shows the curves of the total force versus the overlap (the negative gap) for different damping. It can be seen that similarly to the linear model, the loading and unloading force–gap relations for the ideally elastic case coincide, and in the damped collisions, the loading and unloading curves form a hysteresis loop. This time, unlike in the linear model, the loading and unloading curves are smooth functions for the zero gap.

## *4.3 Walton-Braun Elastoplastic Model*

### Formulation of the model

Viscous damping can be considered as a mechanism representing inelastic particle deformation during particle collision. Plastic deformation is dependent on the dis-

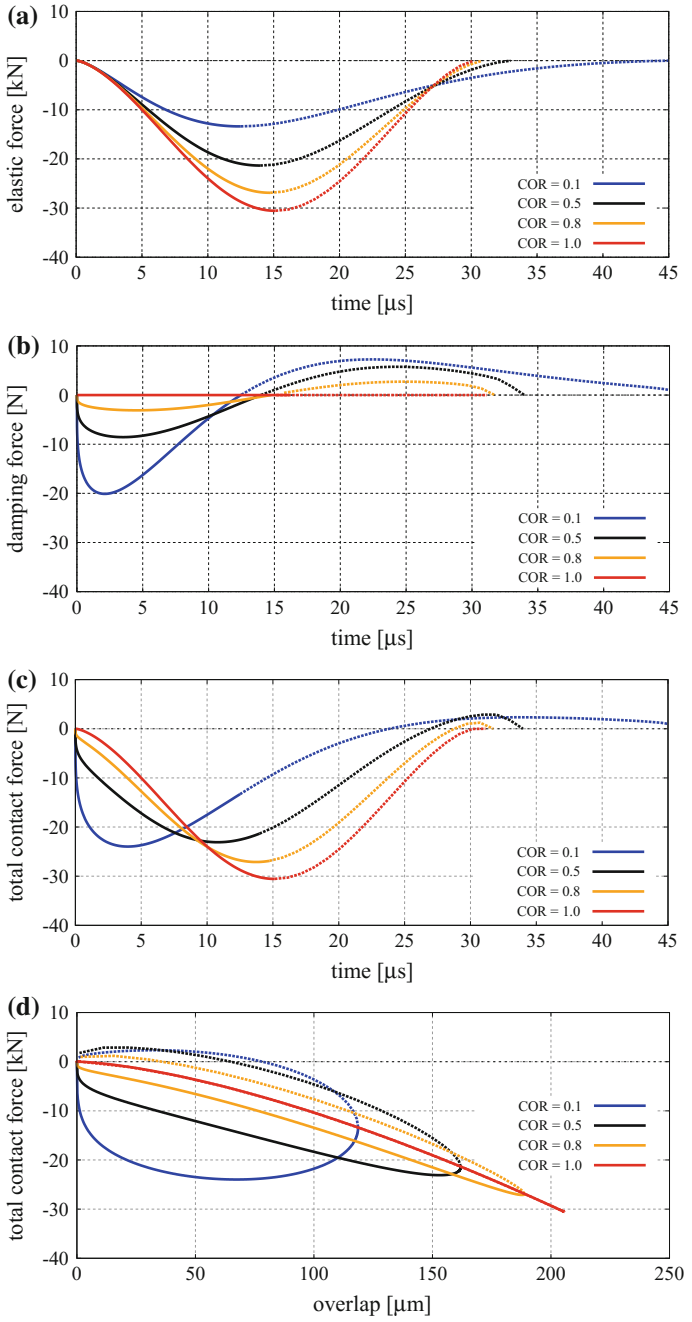


**Fig. 17** Evolution of contact kinematic parameters and contact forces during collision of two balls in the nonlinear Kelvin–Voigt model for different values of COR (the solid parts of the curves represent loading and the broken ones – unloading)

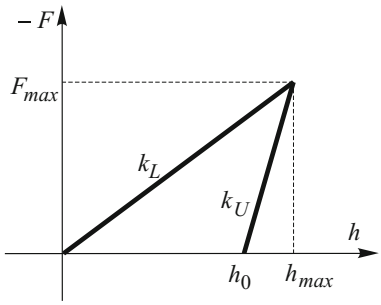


**Fig. 18** Force versus particle overlap in the Walton–Braun model

placement type variable, therefore rate-independent hysteretic contact models such as the model proposed by Walton and Braun (1986) seem to be more appropriate for modelling collisions associated with plastic deformations. The Walton–Braun model assumes a linear force–overlap relationship, but the unloading slope (stiffness) is higher than the loading slope (stiffness), which leads to a certain residual irreversible overlap when the force drops to zero. This allows us to treat this model as elastoplastic with elastic unloading. The force as a function of the particle overlap is plotted in Fig. 18. Please note that although the plot is in the first quadrant of the graph, the convention of the contact force sign (compressive contact force – negative) has been kept by taking the negative of force for the vertical axis. The force is given by:

$$F = \begin{cases} -k_L h & \text{if} \quad h \geq h_{max} \quad \text{(loading)}, \\ -k_U (h - h_0) & \text{if} \quad h_0 < h < h_{max} \quad \text{(un-/reloading)}, \\ 0 & \text{if} \quad 0 < h < h_0 \quad \text{(no contact)}. \end{cases} \tag{76}$$

The residual overlap $h_0$ representing the plastic deformation of the contacting particles can be easily obtained as

$$h_0 = h_{max} \left( 1 - \frac{k_L}{k_U} \right) \tag{77}$$

The reloding path follows the unloading path until the maximum overlap is achieved and the loading path is reactivated.

Energy is dissipated due to spring force hysteresis. The coefficient of restitution $e$, given by

$$e = \sqrt{\frac{k_L}{k_U}}, \tag{78}$$

is independent of the impact velocity, which is in disagreement with experimental observations. A more realistic coefficient of restitution can be obtained using a variable unloading stiffness $k_U$ increasing with the maximum absolute force, $F^{max}$, or the maximum overlap, $h_{max}$, achieved before unloading Walton and Braun (1986), so that:

$$k_U = k_L + SF_{max} \tag{79}$$

or

$$k_U = k_L + Bh_{max}\,, \tag{80}$$

where $S$ and $B$ are certain constants. For the Walton-Braun contact model with variable unloading, the coefficient of restitution depends on the relative velocity of approach $v_r^0$ as follows Walton and Braun, 1986:

$$e = \sqrt{\frac{\omega_0}{Sv_r^0 + \omega_0}}\,, \tag{81}$$

where

$$\omega_0 = \sqrt{\frac{2k_L}{m}}\,. \tag{82}$$

**Numerical example**

*Collision of two balls with given initial velocities*

The Walton–Braun contact model has been applied to simulate a collision of two equal balls of radius $R = 10\,\text{mm}$ and of the same density $\rho = 8000\,\text{kg/m}^3$. The loading stiffness has been assumed $k_L = 1.25 \times 10^8\,\text{N/m}$, which is approximately close to the average stiffness in the Hertzian model (in the considered range) used in the numerical example in Sect. 4.2. The variable unloading stiffness has been taken according to Eq. (79) assuming $S = 10\,1/\text{m}$. The problem has been analysed assuming different initial velocities: $v = 10$, 20, 30 and 40 m/s. The evolution of the gap (overlap) between the balls and the velocity of one of the balls in the analysed cases have been plotted in Fig. 19.

The curves have been plotted for the collision time only (until the residual overlap has been achieved during unloading at each case). The coefficients of restitution for the analysed cases evaluated using the general formula (63) and predicted by the specific formula (81) for the Walton–Braun model are given in Table 1. It can be observed that the values obtained in both ways coincide. It can also be observed the values of the coefficients of restitution decrease with an increase of impact velocity, which agrees with experimental observations.

The contact forces for different impact velocities are plotted as functions of the time and overlap in Fig. 20a and b, respectively. It can be observed in Fig. 20a that the highest the impact velocity is, the shorter the collision time is. Figure 20b shows that the loading stiffness for different velocities is the same and the unloading stiffness increase with the impact velocity since higher maximum forces are achieved for higher velocities. It is assumed that the collision ends when the force during unloading decreases to zero. A certain residual overlap corresponds to this instant.

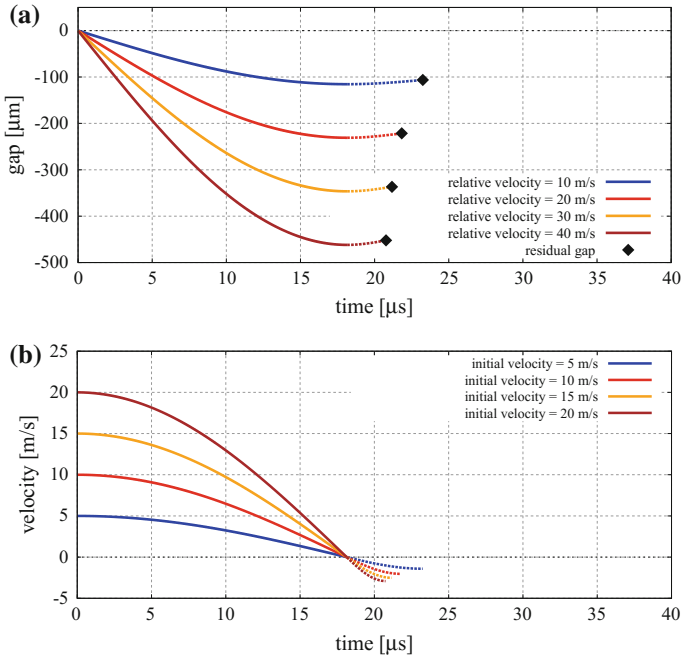


**Fig. 19** Evolution of contact kinematic parameters during the collision of two balls in the Walton–Braun elastoplastic model for different values of impact velocities: **a** evolution of the gap (overlap), **b** evolution of the ball velocity (solid parts of the curves represent the loading and broken parts of the curve – the unloading)

**Table 1** Coefficients of restitution for the Walton–Braun model with variable unloading

| $v^0$ (m/s) | $v_r^0$ (m/s) | $v_r$ (m/s) | $e$, Eq. (63) | $e$, Eq. (81) |
|---|---|---|---|---|
| 5 | 10 | 2.8230 | 0.28230 | 0.28231 |
| 10 | 20 | 4.0744 | 0.20373 | 0.20373 |
| 15 | 30 | 5.0250 | 0.16750 | 0.16750 |
| 20 | 40 | 5.8228 | 0.14557 | 0.14557 |

## *4.4 Storåkers plastic model*

### Formulation of the model

The plastic deformation of the contacting spherical particles has been assumed in the model proposed by Storåkers et al. (1997), Storåkers et al. (1999). This model considers a general viscoplastic behaviour combining strain hardening plasticity and creep. Here, a simplified formulation of the model without strain rate effects will be presented. Such a model has been used by Olsson and Larsson (2012) to study powder compaction.

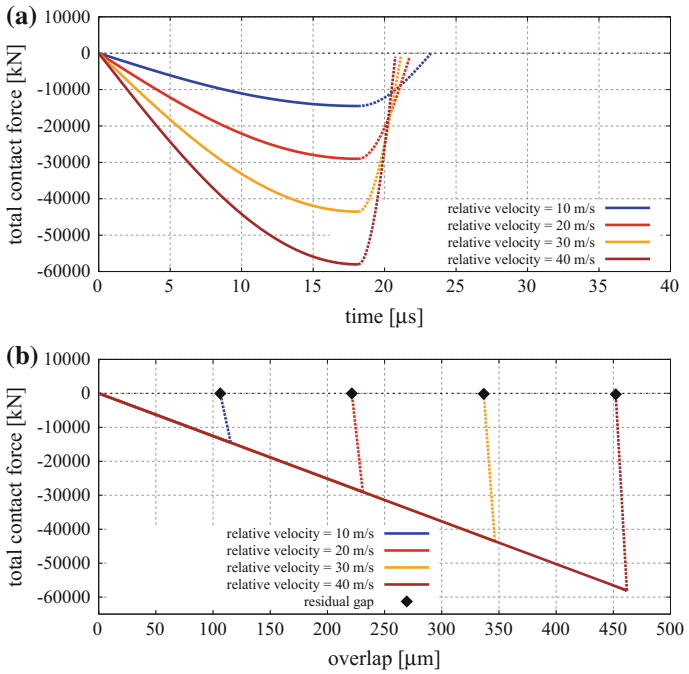


**Fig. 20** Evolution of contact forces during the collision of two balls in the Walton–Braun elasto-plastic model for different values of impact velocities: **a** force versus time, **b** force versus overlap (solid parts of the curves represent the loading and broken parts of the curves – the unloading)

Two particles of radii $R_i$ and $R_j$ are considered. The plastic properties of the particles' material are assumed to follow the Hollomon stress-strain relationship

$$\sigma = \sigma_0 \varepsilon^m \tag{83}$$

where $\sigma_0$ and $m$ are material constants. The normal interaction force $F$ in the Storåkers model is given by the following equation Olsson and Larsson (2012):

$$F = -2^{1-m/2} 3^{1-m} \pi c^{2+m} \sigma_0 (R^*)^{1-m/2} h^{1+m/2}\,, \tag{84}$$

where $R^*$ is the effective radius defined by Eq. (56), $h$ is the particle overlap, the parameter $c$ depends on the strain hardening exponent $m$:

$$c = \sqrt{1.43 \exp(-0.97m)}\,. \tag{85}$$

For the ideal plasticity, when $m = 0$ and $\sigma = \sigma_Y$, Eq. (84) is reduced to:

$$F^p = 6\pi c^2 \sigma_Y R^* h\,, \tag{86}$$

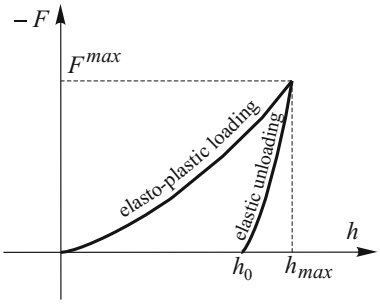


**Fig. 21** Force versus particle overlap in the model combining plastic loading according to the Storakers model with the elastic Hertzian unloading

where $c^2 = 1.43$. The linear relationship (86) provides an expression for the stiffness:

$$k = 6\pi c^2 \sigma_Y R^* , \tag{87}$$

which can be used for the loading in the Walton–Braun model.

The Storåkers model has been derived neglecting elastic deformation, cf. Larsson et al. (1996). In such a model, the unloading would be governed by the rigid behaviour (no change of deformation during the unloading). Assuming that the loading curve is valid for an elastoplastic material Olsson and Larsson (2012) combined the Storåkers model with the elastic unloading according to the Hertz model. The contact force versus particle overlap for this model is plotted schematically in Fig. 21. The force during the elastic unloading as well as for the reloading is given by the formula adapted from Eq. (64):

$$F = -\frac{4}{3} E^* \sqrt{R^*} (h - h_0)^{\frac{3}{2}} , \tag{88}$$

where $h_0$ is obtained from Eq. (88) taking $F^{ep} = F^{max}$ and $h = h_{max}$.

Although the Storåkers model was derived for frictionless contact, it was combined with the regularized Coulomb friction model by Olsson and Larsson (2012).

**Numerical example**

*Contact of two spheres under compressive axial load*

Two equal spheres of radius $R = 10$ mm with plastic properties given by Eq. (83) have been considered assuming different values of hardening exponent $m = 0,\ 0.05,\ 0.1$ and 0.2. The yield stress $\sigma_Y = 200$ MPa has been assumed for the ideal plasticity ($m = 0$). The Hollomon constants $\sigma_0$ corresponding to the strain hardening exponents $m$ have been evaluated assuming that all the curves pass through the point corresponding to the yield point in the elasto-plastic model: $(\sigma_Y/E, \sigma_Y)$ (taking the Young's modulus $E = 200$ GPa). Thus, the following pairs of the Hollomon constants have been determined: ($m = 0$, $\sigma_0 = 800$ MPa), ($m = 0.05$, $\sigma_0 = 1480$ MPa), ($m = 0.1$, $\sigma_0 = 1375$ MPa) and ($m = 0.2$, $\sigma_0 = 2363$ MPa). The corresponding stress–strain curves are plotted in Fig. 22.

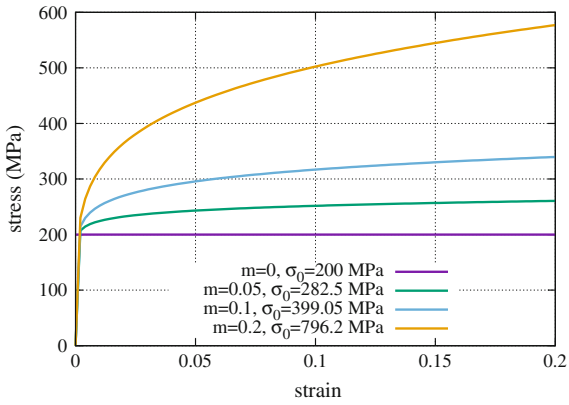


**Fig. 22** Stress–strain curves for different strain hardening

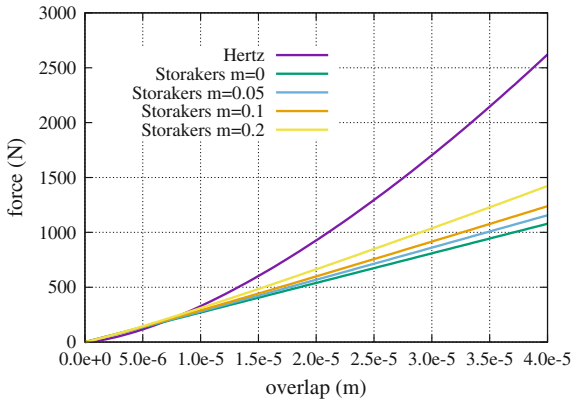


**Fig. 23** Force versus particle overlap in the Storakers model in comparison the Hertz model

The compressive loading has been introduced by prescribing the displacements to the particle centres. The evolution of the contact forces $F$ predicted by Storåkers models as functions of the particle overlap $h$ is shown in Fig. 23 in comparison to the Herz model.

## *4.5 Thornton Elastoplastic Model*

The model proposed by Thornton (1997) considers an interaction of two spheres with elastic-perfectly plastic properties. The interaction includes elastic and elastoplastic loading combined with elastic unloading. The force–overlap relationship for loading and unloading is plotted in Fig. 24.

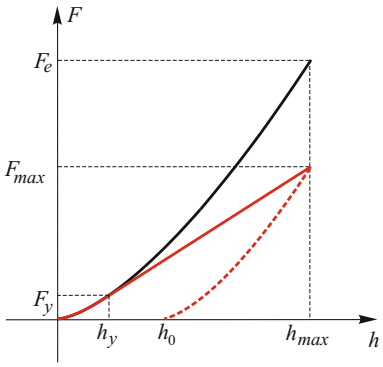


**Fig. 24** Force versus particle overlap in the elasto-plastic Thornton model

### Elastic loading

The contact force $F$ at the initial stage of loading induces elastic deformation at the contact and it is given by the Hertz law, cf. Eqs. (64) and (65):

$$F = \frac{4}{3} E^* \sqrt{R^*} h^{\frac{3}{2}} , \tag{89}$$

where $h$ is the amount the particles overlap, $E^*$ is the effective modulus of elasticity defined by Eq. (66), and $R^*$ is the effective radius defined by Eq. (56).

The Hertzian contact pressure distribution is given by the following relationship:

$$p = p_0 \left[ 1 - \left( \frac{r}{a} \right)^2 \right]^{\frac{1}{2}} , \tag{90}$$

where $a$ is the radius of the contact area, $r$ is the distance from the axis of symmetry and

$$p_0 = \frac{3F}{2\pi a^2} . \tag{91}$$

The contact area radius $a$ is related to the particle overlap $h$ as follows:

$$a^2 = R^* h \tag{92}$$

It is assumed that the loading is purely elastic below a certain value $F_y$ (Fig. 24) corresponding to the initial yielding at the contact – when the maximum contact pressure $p_0$ under an increasing compressive load reaches the yield limit $\sigma_y$, called the *c*ontact yield stress (Fig. 25):

$$p_0(a = a_y) = \sigma_y . \tag{93}$$

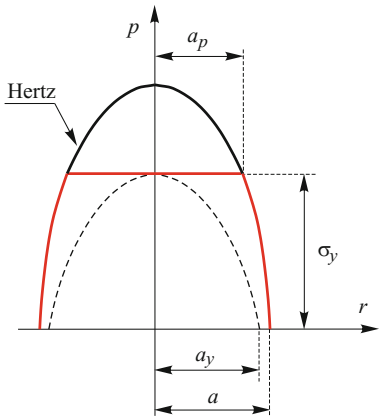


**Fig. 25** Contact pressure distribution in the elasto-plastic Thornton model

Combining Eqs. (89), (91), (92) and (93) we can easily obtain the following formulae for the limit elastic contact force $F_y$ and corresponding overlap $h_y$:

$$F_y = \frac{\pi^3 R^{*2} \sigma_y^3}{6E^{*2}}, \tag{94}$$

$$h_y = \frac{\pi^2 R^* \sigma_y^2}{4E^{*2}}. \tag{95}$$

For the spheres of the same size and with the same properties, Eqs. (94) and (95) have the following form:

$$F_y = \frac{\pi^3 R^2 (1-\nu^2) \sigma_y^3}{6E^2}, \tag{96}$$

$$h_y = \frac{\pi^2 R (1-\nu^2) \sigma_y^2}{2E^2}. \tag{97}$$

It should be remarked that the contact yield stress $\sigma_y$ should not be identified with the uniaxial yield stress $\sigma_Y$. It has been shown by Vu-Quoc et al. (2000) that

$$\sigma_y = A_Y \sigma_Y, \tag{98}$$

where $A_Y$ is a certain parameter dependent on the material properties and yield criterion. For the Huber–Mises criterion and Poisson's ratio $\nu = 0.3$, we obtain $A_Y = 1.61$, for $\nu = 0.4$ we obtain $A_Y = 1.74$.

**Elastoplastic loading**

After the yielding, the contact pressure distribution with the cut-off corresponding to the contact yield stress $\sigma_y$ (see Fig. 25) is assumed. Given the contact pressure

distribution shown in Fig. 25 the contact force can be obtained from the following formula:

$$F = F_e - 2\pi \int_0^{a_p} (p(r) - \sigma_y)\, \mathrm{d}r\,, \tag{99}$$

where $F_e$ is the elastic Hertz force corresponding to the contact area $a$, and the integral term is defined for the area with uniform contact pressure with radius $a_p$. After integrating Eq. (99) with pressure distribution according to Eq. (90) and performing further transformation the linear force–displacement relationship for the plastic loading is obtained in the following form, cf. Thornton (1997):

$$F = F_y + \pi\sigma_y R^*(h - h_y)\,. \tag{100}$$

**Elastic unloading**

It is assumed that the unloading is performed according to the Hertzian law, however, due to plastic deformation the contact curvature is smaller, and the unloading is performed assuming a certain curvature defined by the radius $R_p^*$ $1/R_p^*$ $(1/R_p^* < 1/R^*)$. The radius $R_p^*$ is determined from the assumption that with the contact area developed by the actual force $F_{max}$ and the curvature $1/R_p^*$ is the same as it would be obtained with the curvature $1/R^*$ and the equivalent elastic force $F_e$, which is given by, cf. Fig. 24:

$$F_e = \frac{4}{3} E^* \sqrt{R^*} h_{max}^{\frac{3}{2}}\,, \tag{101}$$

The idea of equivalence of the contact area has been explained in Fig. 26. It can be expressed by the following equivalence:

$$F_{max} R_p^* = F_e R^*\,, \tag{102}$$

Then, the force during unloading is given as follows:

$$F = \frac{4}{3} E^* \sqrt{R_p^*} (h - h_0)^{\frac{3}{2}}\,, \tag{103}$$

The residual overlap $h_0$ can be determined taking Eq. (103) for $h_{max}$

$$h_0 = h_{max} - \left( \frac{3F_{max}}{4E^* \sqrt{R_p^*}} \right)^{\frac{2}{3}}\,. \tag{104}$$

**Numerical examples**

*Collision of two balls with given initial velocities*

Performance of the Thornton model will be demonstrated in simulations of collisions of two equal balls of radius $R = 10\,\mathrm{mm}$. The following properties have been assumed:

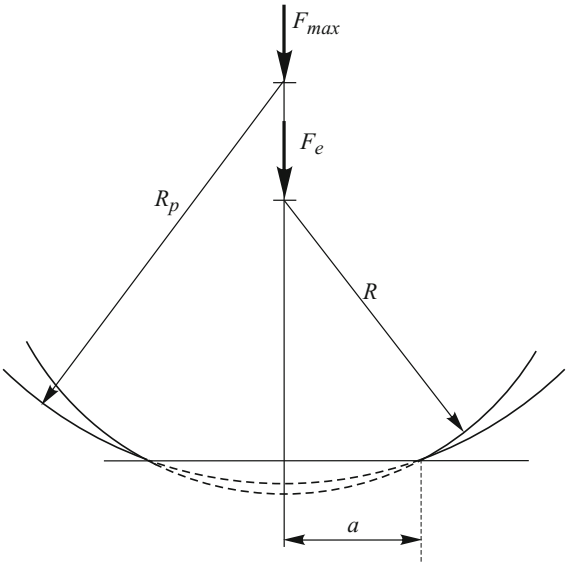


**Fig. 26** Definition of the curvature for the elastic unloading in the elasto-plastic Thornton model

mass density $\rho = 8000\,\text{kg/m}^3$, Young's modulus $E = 200\,\text{GPa}$, Poisson's ratio $nu = 0.3$, and the contact yield stress $\sigma_y = 200\,\text{MPa}$. The problem has been analysed for different values of velocities in two ranges – lower velocities: 0.005, 0.010 and 0.015 m/s, and higher velocities: 0.5, 0.1 and 1.5 m/s.

The results for the lower velocities are presented in Figs. 27 and 28, and the results for the higher velocities in Figs. 29 and 30. The evolution of the gap between the balls and the velocity of one of the balls for lower velocities have been plotted in Fig. 27a and b. It can be seen that the lower the impact velocity is, the longer the impact is. The coefficients of restitution for the analysed cases evaluated using the general formula (63) are given in Table 2. It can be observed that the values of the coefficients of restitution decrease with an increase of impact velocity, which agrees with experimental observations.

The contact forces for lower impact velocities are plotted as functions of the time and overlap in Fig. 28a and b, respectively. It can be observed in Fig. 28a that the highest the impact velocity is, the shorter the collision time is. Figure 28b shows that the loading curve for different velocities is the same for different velocities. It can be observed in Fig. 28b that the incipient yielding occurs at a very early stage of loading therefore a very small part of the loading is purely elastic. Most of the loading is characterized by a linear relationship given by Eq. (99). The nonlinear force–displacement relationship is observed for the unloading for lower velocities. The results for higher velocities plotted in Fig. 30 show that practically the whole range of loading is characterized by the linear force–displacement relationship, and the unloading is very close to a linear behaviour. This shows that a linear elastoplastic model such as the Walton–Braun model can be sufficiently accurate for higher impact velocities or higher forces.

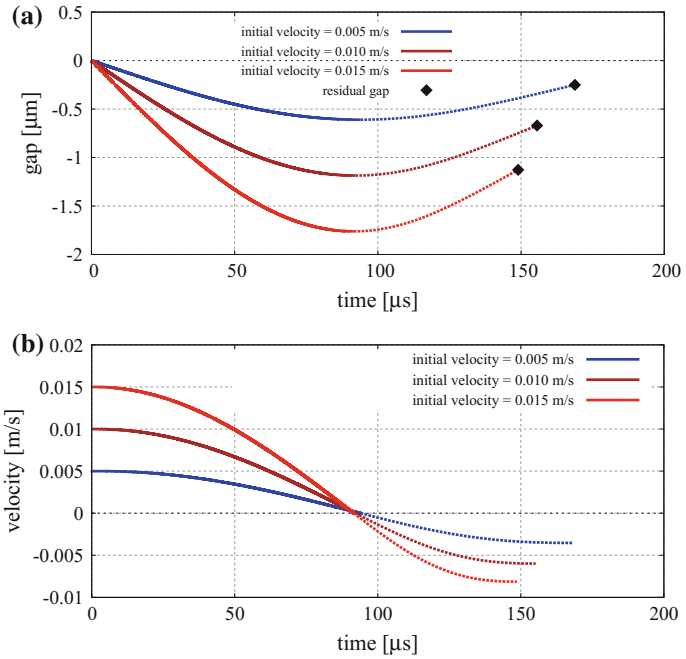


**Fig. 27** Evolution of contact kinematic parameters during the collision of two balls in the Thornton elastoplastic model in a range of low impact velocities: **a** evolution of the gap, **b** evolution of the ball velocity (solid parts of the curves represent the loading and broken parts of the curve – the unloading)

## *4.6 Cohesive Elastic–perfectly Brittle Model*

Modelling of cohesive materials such as rocks or concrete requires a model which takes into account a tensile interaction between discrete elements. This model assumes cohesive bonding between neighbouring particles. These bonds can be broken under load allowing us to simulate initiation and propagation of material fracture. After decohesion, standard cohesionless contact conditions are assumed.

Contact laws for the normal and tangential direction for the elastic perfectly brittle model are shown in Fig. 31. When two particles are bonded the contact forces in both normal and tangential directions are calculated from the linear constitutive relationships:

$$F_{\mathrm{n}}^{\mathrm{cont}} = k_{\mathrm{n}} g \,, \tag{105}$$

$$\boldsymbol{F}_{\mathrm{t}}^{\mathrm{cont}} = k_{\mathrm{t}}\, \boldsymbol{u}_{\mathrm{rt}} \,, \tag{106}$$

where: $F_{\mathrm{n}}^{\mathrm{cont}}$ – normal contact force, $\boldsymbol{F}_{\mathrm{t}}^{\mathrm{cont}}$ – tangential contact force, $k_{\mathrm{n}}$ – interface stiffness in the normal direction, $k_{\mathrm{t}}$ – interface stiffness in the tangential direction,

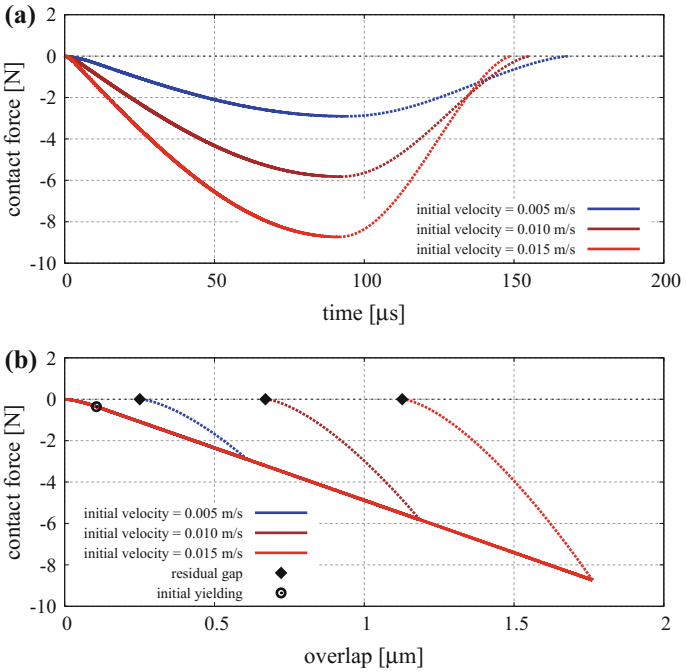


**Fig. 28** Evolution of contact forces during the collision of two balls in the Thornton elastoplastic model for a range of low impact velocities: **a** force versus time, **b** force versus overlap (solid parts of the curves represent the loading and broken parts of the curves – the unloading)

$g$ – gap/overlap, $\boldsymbol{u}_{\mathrm{rt}}$ – tangential relative displacement. It should be remarked that unlike Eq. (38), formula (105) is used for both negative and positive values of the gap $g$.

Cohesive bonds are broken instantaneously when the interface strength is exceeded in the tangential direction by the tangential contact force or in the normal direction by the tensile contact force. The failure (decohesion) criterion can be written as:

$$F_{\mathrm{n}}^{\mathrm{cont}} \leq R_{\mathrm{n}}\,, \tag{107}$$

$$\|\boldsymbol{F}_{\mathrm{t}}^{\mathrm{cont}}\| \leq R_{\mathrm{t}}\,, \tag{108}$$

where: $R_{\mathrm{n}}$ — interface strength in the normal direction, $R_{\mathrm{t}}$ — interface strength in the tangential direction.

In the absence of cohesion the normal contact force can be compressive only ($R_n \leq 0$) and tangential contact force can be nonzero due to friction if $R_{\mathrm{n}} < 0$ or zero otherwise. The friction force is evaluated according to the regularized Coulomb friction model.

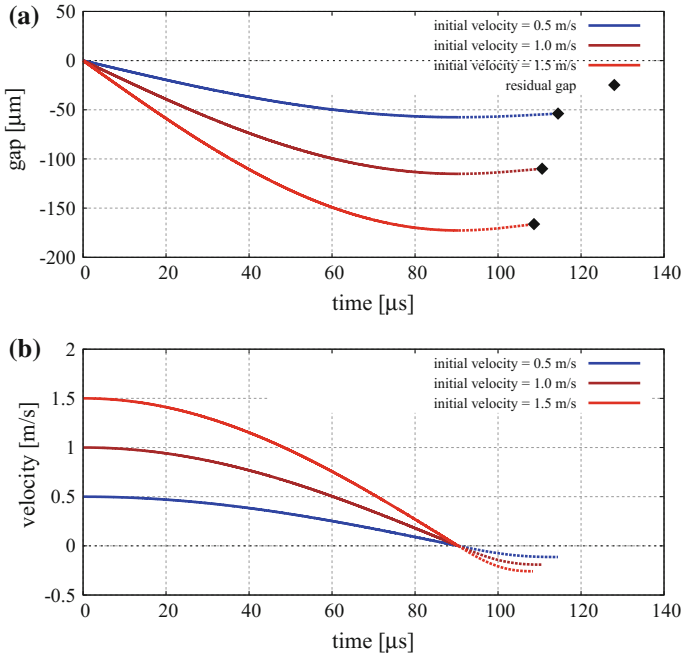


**Fig. 29** Evolution of contact kinematic parameters during the collision of two balls in the Thornton elastoplastic model in a range of higher impact velocities: **a** evolution of the gap, **b** evolution of the ball velocity (solid parts of the curves represent the loading and broken parts of the curve – the unloading)

## 5 Moment Type Interaction

Contact model in the discrete element method except for forces can include a moment type interaction (Wang et al. 2015). In a general case, there can be a moment interaction between bonded and unbonded particles. Here, the moment type interaction between unbonded particles will be presented.

A moment type interaction allows to compensate deficiencies of the discrete element model due to an idealized shape of spherical particles. It provides resistance to a relative rotation of contacting particles (discrete elements). The relative motion of two particles $i$ and $j$ can be described by a relative angular velocity $\boldsymbol{\omega}_{\mathrm{r}}$ given by

$$\boldsymbol{\omega}_{\mathrm{r}} = \boldsymbol{\omega}_i - \boldsymbol{\omega}_j \,. \tag{109}$$

The relative angular velocity $\boldsymbol{\omega}_{\mathrm{r}}$ can be decomposed into the components normal and tangent to the contact plane, $\boldsymbol{\omega}_{\mathrm{rn}}$ and $\boldsymbol{\omega}_{\mathrm{rt}}$, respectively:

$$\boldsymbol{\omega}_{\mathrm{r}} = \boldsymbol{\omega}_{\mathrm{rn}} + \boldsymbol{\omega}_{\mathrm{rs}} = \omega_{\mathrm{rn}} \cdot \boldsymbol{n} + \boldsymbol{\omega}_{\mathrm{rs}} \,. \tag{110}$$

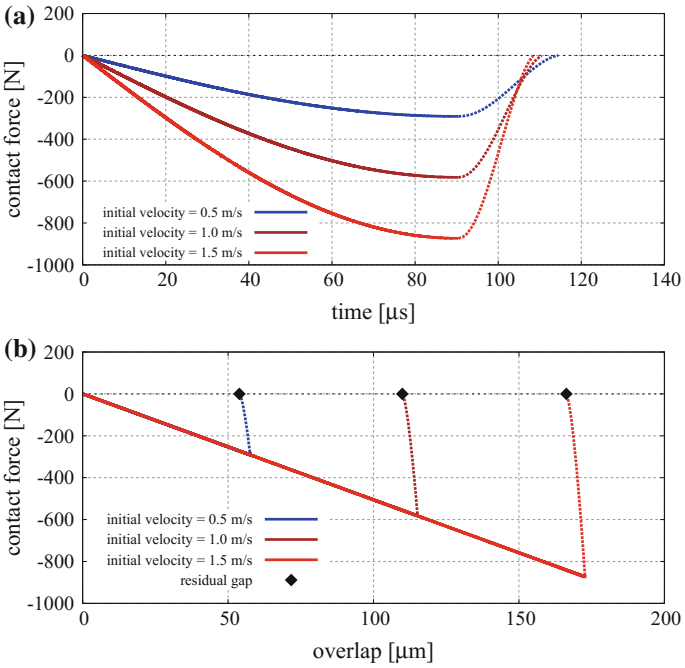


**Fig. 30** Evolution of contact forces during the collision of two balls in the Thornton elastoplastic model for a range of higher impact velocities: **a** force versus time, **b** force versus overlap (solid parts of the curves represent the loading and broken parts of the curves – the unloading)

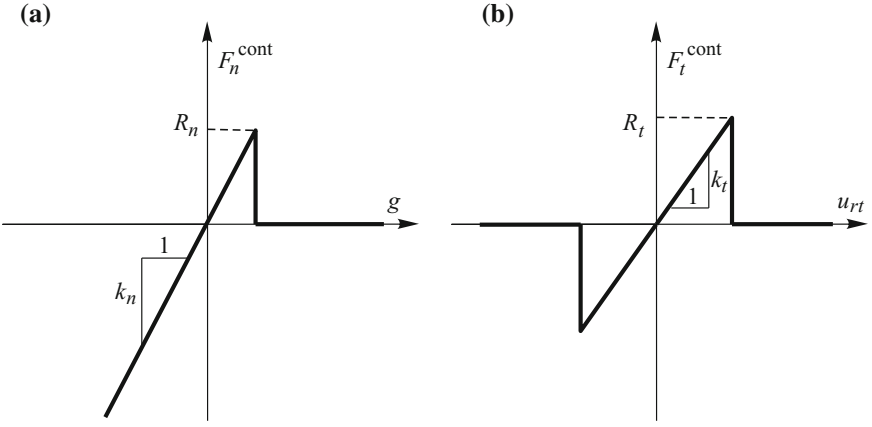


**Fig. 31** Force–displacement relationships for the elastic perfectly brittle model: **a** in the normal direction, **b** in the tangential direction

**Table 2** Coefficients of restitution for the Thornton model

| $v^0$ (m/s) | $v^0_{rel}$ (m/s) | $v_{rel}$ (m/s) | $e$, Eq. (63) |
|---|---|---|---|
| 0.005 | 0.010 | 0.00706 | 0.7060 |
| 0.010 | 0.020 | 0.01197 | 0.5987 |
| 0.015 | 0.030 | 0.01627 | 0.5424 |
| 0.5 | 1.0 | 0.2269 | 0.2269 |
| 1.0 | 2.0 | 0.3815 | 0.1908 |
| 1.5 | 3.0 | 0.51717 | 0.1724 |

The normal component can be obtained by projection of the velocity vector $\boldsymbol{\omega}_\mathrm{r}$ onto the unit normal vector $\boldsymbol{n}$:

$$\omega_\mathrm{rn} = \boldsymbol{\omega}_\mathrm{r} \cdot \boldsymbol{n} \,. \tag{111}$$

Then, the tangent component is obtained from Eq. (110) as follows

$$\boldsymbol{\omega}_\mathrm{rs} = \boldsymbol{\omega}_\mathrm{r} - \omega_{rn}\boldsymbol{n} \,. \tag{112}$$

The motion defined by the tangent component $\boldsymbol{\omega}_\mathrm{rn}$ is called rolling, and that defined by the normal component $\boldsymbol{\omega}_\mathrm{rt}$ is referred to as twisting.

Analogously, the contact interaction moment $\boldsymbol{T}^c$ between the particles can be decomposed into two components – normal and tangential to the contact plane, $\boldsymbol{T}_\mathrm{n}$ i $\boldsymbol{T}_\mathrm{s}$, respectively:

$$\boldsymbol{T}^c = \boldsymbol{T}_\mathrm{n} + \boldsymbol{T}_\mathrm{s} = T_\mathrm{n}\,\boldsymbol{n} + \boldsymbol{T}_\mathrm{s} \,. \tag{113}$$

Models of twisting and rolling resistance can be defined analogously to sliding friction models. A model of twisting resistance can be defined in terms of the angular velocity component $\boldsymbol{\omega}_\mathrm{rn}$ and the component $\boldsymbol{T}_\mathrm{n}$ of the contact moment.

For the model of twisting resistance the Kuhn–Tucker conditions can be written analogously to the conditions (22) as follows:

$$\phi_\mathrm{n} \le 0 \,, \quad \lambda_\mathrm{n} \ge 0 \,, \quad \phi_\mathrm{n}\lambda_\mathrm{n} = 0 \,, \tag{114}$$

where $\lambda_\mathrm{n}$ is defined by the non-associated rolling law:

$$\boldsymbol{\omega}_\mathrm{rn} = \lambda_\mathrm{n} \frac{\boldsymbol{T}_\mathrm{n}}{||\boldsymbol{T}_\mathrm{n}||} \,, \tag{115}$$

and $\phi_\mathrm{n}$ is given by the following equation:

$$\phi_\mathrm{n} = \|\boldsymbol{T}_\mathrm{n}\| - a_\mathrm{n}\mu|F_\mathrm{n}| \,, \tag{116}$$

$a_\mathrm{n}$ is a parameter which has dimension of length determining the limit moment of twisting resistance. It has been assumed that this moment is proportional to the normal contact force $F_\mathrm{n}$ and Coulomb friction coefficient $\mu$.

Analogously, a model of rolling resistance can be defined. The Kuhn–Tucker conditions for the model of rolling resistance can be written as follows:

$$\phi_\mathrm{s} \leq 0\,, \quad \lambda_\mathrm{s} \geq 0\,, \quad \phi_\mathrm{s}\lambda_\mathrm{s} = 0\,, \tag{117}$$

where $\lambda_\mathrm{s}$ is defined by the non-associated law of rolling:

$$\boldsymbol{\omega}_\mathrm{rs} = \lambda_\mathrm{s} \frac{\boldsymbol{T}_\mathrm{s}}{||\boldsymbol{T}_\mathrm{s}||}\,, \tag{118}$$

and $\phi_\mathrm{s}$ is given by

$$\phi_\mathrm{s} = \|\boldsymbol{T}_\mathrm{s}\| - a_\mathrm{s}|F_\mathrm{n}|\,, \tag{119}$$

where the limit moment of rolling resistance. depends on the normal contact force $F_\mathrm{n}$ and the parameter $a_\mathrm{s}$ which has dimension of length. This definition is consistent with the concept of rolling friction employed in engineering, where the parameter $a_\mathrm{s}$ is called the coefficient of rolling friction.

The conditions (114)–(116) and (117)–(119) can be regularized introducing the penalty coefficients $k_\mathrm{n}^\mathrm{rot}$ and $k_\mathrm{s}^\mathrm{rot}$ into the twisting and rolling laws (115) and (118)

$$\dot{\boldsymbol{T}}_n = k_\mathrm{n}^\mathrm{rot}\left(\boldsymbol{\omega}_\mathrm{rn} - \lambda_\mathrm{n}\frac{\boldsymbol{T}_\mathrm{n}}{||\boldsymbol{T}_\mathrm{n}||}\right)\,, \tag{120}$$

$$\dot{\boldsymbol{T}}_\mathrm{s} = k_\mathrm{s}^\mathrm{rot}\left(\boldsymbol{\omega}_\mathrm{rs} - \lambda_\mathrm{s}\frac{\boldsymbol{T}_\mathrm{s}}{||\boldsymbol{T}_\mathrm{s}||}\right)\,. \tag{121}$$

After regularization the models of twisting and rolling resistance are similar to elasto-plastic models with non-associated plastic flow rules, and the penalty coefficients play roles of the moduli of elasticity.

## 6 Discrete Element Method for Thermal and Thermomechanical Problems

In many problems, the contact is associated with thermal effects such as heat generation through friction or heat transfer at the contact between particles with different temperatures. The discrete element method can be extended to model thermal and thermomechanical problems.

## 6.1 Formulation of the Discrete Element Method for Heat Conduction Problem

Thermal formulation of the discrete element method introduced here is based on the assumption that the temperature difference inside particles is negligible and the temperature can be considered uniform within particles. Following this assumption heat conduction inside particles is neglected whereas heat transfer to and from particles through their boundary is considered. Such a simplification of the heat conduction problem is typical for the lumped capacitance model, also called the lumped system analysis (Cengel 2007). This assumption is justified for the discrete element model employing relatively small particles and it is consistent with the formulation of the mechanical problem. Similarly as the mechanical problem is governed by the contact interaction, the heat conduction problem is governed by the conductive heat transfer at the particle contacts.

The schematic of the heat transfer for a single particle is shown in Fig. 32. The thermal model is expressed mathematically by the heat balance equation, which can be written for a single particle in the following form:

$$m_i c_i \dot{\theta}_i = Q_i \,, \tag{122}$$

where: $m_i$ – particle mass, $c_i$ – specific heat, $\theta_i$ – particle temperature, $Q_i$ – heat sources or heat fluxes per single particle. $Q_i$ includes externally supplied heat source $Q_i^{\text{ext}}$, heat generated internally within the particle $Q_i^{\text{gen}}$, heat conducted through the contact interface $Q_{ij}^{\text{cont}}$, and convective and radiative heat transfer between particles and environment on the free surface, $Q_i^{\text{conv}}$ and $Q_i^{\text{rad}}$

$$Q_i = Q_i^{\text{ext}} + Q_i^{\text{gen}} + \sum_{j=1}^{n_c} Q_{ij}^{\text{cont}} + Q_i^{\text{conv}} + Q_i^{\text{rad}} \tag{123}$$

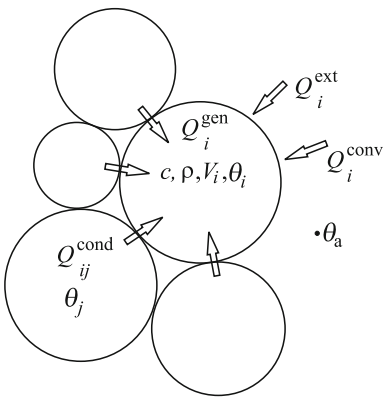


**Fig. 32** Schematic of the heat conduction problem for a discrete element (reproduced from Rojek (2014))

where $n_c$ is the number of particles being in contact with the $i$-th particle.

## 6.2 Model of Thermal Contact

When two solid bodies of different temperature come into contact heat flows from the body with higher temperature to the body with lower temperature until a thermal equilibrium is achieved. If we take two particles with masses $m_i$ and $m_j$, heat capacities $c_i$ and $c_j$, and temperatures $\theta_i$ and $\theta_j$, and bring them into contact, if there no heat exchange with exterior, the thermal equilibrium is achieved at the temperature $\theta$ given by

$$\theta = \frac{m_i c_i \theta_i + m_j c_j \theta_j}{m_i c_i + m_j c_j} \tag{124}$$

The time necessary to reach equilibrium depends on the heat flux through the contact interface $Q_{ij}^{\text{cont}}$ (in J/s). It is commonly assumed that the the heat flux through the contact interface is proportional to the temperature jump $(\theta_i - \theta_j)$, contact area $A^{\text{cont}}$, and a certain coefficient $h^{\text{cont}}$ called thermal contact conductance (Cooper et al. 1969):

$$Q_{ij}^{\text{cont}} = -h^{\text{cont}} A^{\text{cont}} (\theta_i - \theta_j) \tag{125}$$

The contact area $A^{\text{cont}}$ can be related to the local particle size

$$A^{\text{cont}} = \beta R^{*2} \tag{126}$$

where $R^*$ is the equivalent radius defined by Eq. (56) and $\beta$ is a certain dimensionless parameter which should be calibrated for a given discrete element model.

It is sometimes convenient to express heat transfer at the contact in terms of one parameter $H^{\text{cont}} = h^{\text{cont}} A^{\text{cont}}$, then Eq. (125) can be rewritten as Zhang et al. (2011):

$$Q_{ij}^{\text{cont}} = -H^{\text{cont}} (\theta_i - \theta_j) \tag{127}$$

In general case of a contact of different bodies or particles, the thermal contact conductance is dependent on the surface roughness, material properties, interface temperature and interface pressure (Cooper et al. 1969. In the discrete element model, however, the thermal contact conductance $h^{\text{cont}}$ does not represent the thermal resistance of the interface, only, but it should also take into account the influence of the thermal conductivity $\lambda$ ot the particle material. It should be treated as a micromechanical parameter which should give required macroscopic properties of the bulk material.

## 6.3 Time Integration of the Discrete Element Method for Thermal Problem

Heat conduction Eq. (133) can be integrated in time using the explicit forward Euler scheme

$$\theta_i^{n+1} = \theta_i^n + \frac{Q_i^n \Delta t}{m_i c} . \tag{128}$$

The explicit time integration scheme expressed by Eq. (128) is conditionally stable. The time integration step is limited by the critical step $\Delta t_{\text{cr}}^{\text{therm}}$ which can be estimated by the critical value for the one-dimensional heat conduction problem (Hughes 1987)

$$\Delta t_{\text{cr}}^{\text{therm}} \approx \frac{l_{\min}}{2a} , \tag{129}$$

where $l_{\min}$ is the minimum particle centre distance and $s$ is the thermal diffusivity

$$a = \frac{\lambda}{\rho c} . \tag{130}$$

## 6.4 Formulation of the Discrete Element Method for a Coupled Thermo-Mechanical Problem

The mechanical and thermal phenomena can be analysed jointly as a coupled thermo-mechanical problem using the discrete element model (Rojek 2014). Thermo-mechanical problem defined in the framework of the discrete element method by the system of coupled equations formed by the equations of motion (1) and (2) and the heat balance equation (122)

$$m_i \ddot{\boldsymbol{u}}_i = \boldsymbol{F}_i , \tag{131}$$

$$J_i \dot{\boldsymbol{\omega}}_i = \boldsymbol{T}_i , \tag{132}$$

$$m_i c \dot{\theta}_i = Q_i \tag{133}$$

with appropriate initial conditions. Coupling of Eqs. (131) and (132) with Eq. (133) can be obtained considering such effects as:

- frictional heat generation,
- thermal expansion of the particles and its effect on particle interaction (thermal stresses),
- temperature dependence of mechanical contact parameters (due to temperature dependence of material macroscopic properties),
- modification of the geometrical configuration of thermal problem determined by the solution of mechanical problem.

## 6.5 Thermomechanical Contact

Friction considered in the mechanical problem is associated with heat generation. The heat is absorbed by the particles increasing their temperature and can be conducted to other particles by heat transfer at the contact. These coupled phenomena can be taken into account in the contact model considered in the formulation of the thermomechanical model. The schematic of the thermomechanical contact model is shown schematically in Fig. 33.

Heat generation through frictional dissipation is calculated using the following formula

$$Q^{\text{gen}} = \chi \, |F_{\text{t}} \, v_{\text{rt}}^{\text{ir}}| \, , \tag{134}$$

where $F_{\text{t}}$ is the friction force, $v_{\text{rt}}^{\text{ir}}$ is the irreversible part of the relative tangential velocity, and $0 \leq \chi \leq 1$ is the part of the friction work converted to heat. Heat generated at the contact point is absorbed by the contacting particles

$$Q^{\text{gen}} = Q_{ij}^{\text{gen}} + Q_{ji}^{\text{gen}} \tag{135}$$

If the particles are of the same materials, it is assumed that the heat is absorbed equally by the particles:

$$Q_{ij}^{\text{gen}} = Q_{ji}^{\text{gen}} = 0.5 Q^{\text{gen}} \tag{136}$$

In a general case, when the particle thermal properties can be different, heat absorbed by each of the contacting particles is assumed to be proportional to the thermal effusivity of the particle materials

$$\frac{Q_{ij}^{\text{gen}}}{Q_{ji}^{\text{gen}}} = \frac{\alpha Q^{\text{gen}}}{(1-\alpha) Q^{\text{gen}}} = \frac{e_i}{e_j} \tag{137}$$

with the effusivity $e$ being defined as

$$e = \sqrt{\lambda \rho c} \tag{138}$$

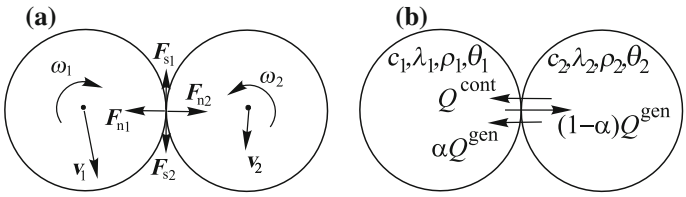


**Fig. 33** Thermomechanical contact schematic for a pair of particles: **a** mechanical contact interaction, **b** thermal contact effects (reproduced from Rojek (2014))

where $\lambda$ is the thermal conductivity, $c$ is the specific heat capacity, and $\rho$ is the density. The heat partition coefficient $\alpha$ is given by the following equation

$$\alpha = \frac{e_i}{e_i + e_j} \tag{139}$$

**Solution of Thermomechanical Coupled Problem in the Discrete Element Method**

The system of coupled equations is solved using the staggered solution scheme, in which the mechanical and thermal problems are analysed separately.

1. Solution of the mechanical problem.
   Equations (131) and (132) are integrated in time using the explicit central difference scheme. Employing the equations for the known configuration at the time $t_n$ the solution for the time $t_{n+1}$ is obtained in the following way:

$$\ddot{\boldsymbol{u}}_i^n = \frac{\boldsymbol{F}_i^n}{m_i}\,, \tag{140}$$

$$\dot{\boldsymbol{u}}_i^{n+1/2} = \dot{\boldsymbol{u}}_i^{n-1/2} + \ddot{\boldsymbol{u}}_i^n \Delta t\,, \tag{141}$$

$$\boldsymbol{u}_i^{n+1} = \boldsymbol{u}_i^n + \dot{\boldsymbol{u}}_i^{n+1/2} \Delta t\,, \tag{142}$$

$$\dot{\boldsymbol{\omega}}_i^n = \frac{\boldsymbol{T}_i^n}{J_i}\,, \tag{143}$$

$$\boldsymbol{\omega}_i^{n+1/2} = \boldsymbol{\omega}_i^{n-1/2} + \dot{\boldsymbol{\omega}}_i^n \Delta t\,, \tag{144}$$

$$\Delta\psi_i = \boldsymbol{\omega}_i^{n+1/2} \Delta t\,. \tag{145}$$

   Thermal expansion of the particles and resulting thermal components of the interaction forces are considered in the solution of the mechanical problem. In many problems, thermally induced stresses may material damage or failure (Wanne 2009; Leclerc et al. 2018). Heat generated by friction is evaluated in Eqs. (131) and (132) and passed to Eq. (133).
2. Solution of the thermal problem
   Heat conduction Eq. (133) is integrated in time using the explicit forward Euler scheme

$$\theta_i^{n+1} = \theta_i^n + \frac{Q_i^n \Delta t}{m_i c}\,. \tag{146}$$

   The thermal problem is solved on the modified particle configuration determined in the solution of the mechanical problem. Particle temperatures evaluated in the solution of the thermal problem are passed to the solution of the mechanical problem.

The explicit time integration scheme of the coupled thermomechanical problem is conditionally stable. The time integration step is limited by the critical step $\Delta t_{\mathrm{cr}}$:

$$\Delta t_{\mathrm{cr}} = \min(\Delta t_{\mathrm{cr}}^{\mathrm{mech}}, \Delta t_{\mathrm{cr}}^{\mathrm{therm}}), \tag{147}$$

where $\Delta t_{\mathrm{cr}}^{\mathrm{mech}}$ is the critical time step for the solution of the mechanical problem depending on the highest eigenfrequency of the discrete system $\Omega_{\max}$

$$\Delta t_{\mathrm{cr}}^{\mathrm{mech}} = \frac{2}{\Omega_{\max}}, \tag{148}$$

and $\Delta t_{\mathrm{cr}}^{\mathrm{therm}}$ is the critical time step for the solution of the thermal problem. The critical time step for the solution of the thermal problem can be estimated according to Eq. (129).

**Concluding remarks**

A brief overview of the basic concepts of the discrete element method and most popular contact models used in this method has been made in this chapter. Contact models used in the DEM intend to reproduce complex phenomena associated with contact between particles (discrete elements) using models composed of relatively simple rheological elements reproducing elementary contact mechanisms.

Many applications of the DEM show that even with simple contact models, it is possible to reproduce the complex macroscopic behaviour of the bulk material modelled by a collection of discrete elements. The contact model in the DEM plays a role of a constitutive model at the micro- or mesoscopic level. The DEM can be used to model cohesionless granular materials as well as various cohesive materials. The DEM in a simple way takes into account discontinuities existing in the material or occurring under loading. The DEM is a suitable tool to model failure of materials and structures characterized by multiple fracturing.

It must be remarked that the DEM is not a simple method for a user. The choice of a suitable contact model and evaluation of appropriate model parameters requires a certain experience and knowledge. The author dares hope this work will be useful to understand the physical background and mathematical representation of the contact phenomena in the DEM.

**Acknowledgements** The author would like to thank Mr. Nikhil Madan for performing simulations and preparing the plots for the numerical examples included in this chapter.

## References

J. Argyris. An excursion into large rotations. *Comput. Meth. Appl. Mech. Eng.*, 32: 85–155, 1982.

J.P. Bardet and J. Proubet. A numerical investigation of the structure of persistent shear bands in granular media. *Geotechnique*, 41: 599–613, 1991.

T. Belytschko, P. Smolinski, and W.K. Liu. Stability of multi-time step partitioned integrators for the first order finite element systems. *Comput. Meth. Appl. Mech. Eng.*, 49: 281–297, 1985.

Y.A. Cengel. *Heat and Mass Transfer: A Practical Approach*. McGraw-Hill, Third Edition edition, 2007.

M.G. Cooper, B.B. Mikic, and M.M. Yovanovich. Thermal contact conductance. *Int. J. Heat Mass Transfer*, 12: 279–300, 1969.

P.A. Cundall. A Computer Model for Simulating Progressive Large Scale Movements in Blocky Rock Systems. In *Proc. Int. Symp. Rock Fracture, ISRM*, pages 2–8, Nancy, France, 1971.

P.A. Cundall. Distinct element models of rock and soil structure. In *Analytical and computational models in engineering and rock mechanics*. Allen&Unwin, London, 1987.

P.A. Cundall. Formulation of a Three Dimensional Distinct Element Model — Part I. A Scheme to Detect and Represent Contacts in a System of Many Polyhedral Blocks. *Int. J. Rock Mech., Min. Sci. & Geomech. Abstr.*, 25 (3): 107–116, 1988.

P.A. Cundall and O.D.L. Strack. A discrete numerical method for granular assemblies. *Geotechnique*, 29: 47–65, 1979.

A. Curnier. Unilateral contact. mechanical modelling. In P. Wriggers and P. Panagiotopoulos, editors, *New Developments in Contact Problems*, pages 1–54. Springer, 1999.

F. Fleissner, T. Gaugele, and P. Eberhard. Applications of the discrete element method in mechanical engineering. *Multibody Syst. Dyn.*, 18: 81–94, 2007.

P.K. Haff and B.T. Werner. Collisional interaction of a small number of confined inelastic grains. In T. Ariman and T. N. Veziroglu, editors, *Colloidal and Interfacial Phenomena*, pages 483–501. Hemisphere Publishing, 1987.

S. Hentz, L. Daudeville, and F.V. Donzé. Identification and validation of a discrete element model for concrete. *ASCE J. Eng. Mech.*, 130: 709–719, 2004.

H. Hertz. Über die Berührung fester elastischer Körper (On the contact of elastic bodies). *J. Reine Angewandte Math.*, 94: 156–171, 1882.

D.C. Hong and J.A. McLennan. Molecular dynamics simulations of hard sphere granular particles. *Phys. A: Stat. Mech. Applicat.*, 187: 159–171, 1992.

T.J.R. Hughes. *The Finite Element Method. Linear Static and Dynamic Analysis*. Prentice-Hall, 1987.

K.H. Hunt and F.R.E. Crossley. Coefficient of restitution interpreted as damping in vibroimpact. *Journal of Applied Mechanics*, 42: 440, 1975.

R. Jankowski. Analytical expression between the impact damping ratio and the coefficient of restitution in the non-linear viscoelastic model of structural pounding. *Earthquake Engng Struct. Dyn.*, 35: 517–524, 2006.

K.J. Johnson. *Contact Mechanics*. Cambridge University Press, 1985.

G.R. Joldes, A. Wittek, and K. Miller. An adaptive Dynamic Relaxation method for solving nonlinear finite element problems. Application to brain shift estimation. *Int. J. Numer. Method Biomed. Eng.*, 27: 173–185, 2011.

A. Klarbring. Contact, friction, discrete mechanical structures and mathematical programming. In P. Wriggers and P. Panagiotopoulos, editors, *New Developments in Contact Problems*, pages 56–100. Springer, 1999.

H. Kruggel-Emden, S. Wirtz, and V. Scherer. A study on tangential force laws applicable to the discrete element method (DEM) for materials with viscoelastic or plastic behavior. *Chemical Engineering Science*, 63: 1523–1541, 2008.

P.-L. Larsson, S. Biwa, and B. Storåkers. Analysis of cold and hot isostatic compaction of spherical particles. *Acta mater.*, 44: 3655–3666, 1996.

W. Leclerc, H. Haddad, and M. Guessasma. On a discrete element method to simulate thermal-induced damage in 2d composite materials. *Computers and Structures*, 196: 277–291, 2018.

J. Lee. Density waves in the flows of granular media. *Phys. Rev. E*, 49 (1): 281, 1994.

Y.-Y. Lin and C.Y. Hui. Mechanics of contact and adhesion between viscoelastic spheres: An analysis of hysteresis during loading and unloading. *Journal of Polymer Science: Part B: Polymer Physics*, 40: 772–793, 2002.

F.P. Di Maio and A. Di Renzo. Modelling particle contacts in distinct element simulations. Linear and non-linear approach. *Chemical Engineering Research and Design*, 83(A11): 1287–1297, 2005.

I. Marczewska, J. Rojek, and R. Kačianauskas. Investigation of the effective elastic parameters in the discrete element model of granular material by the triaxial compression test. *Archives of Civil and Mechanical Engineering*, 16: 64–75, 2016.

C.L. Martin, D. Bouvard, and S. Shima. Study of particle rearrangement during powder compaction by the Discrete Element Method. *J. Mech. Phys. Solids*, 51: 667–693, 2003.

R.D. Mindlin and H. Deresiewicz. Elastic spheres in contact under varying oblique forces. *ASME Journal of Applied Mechanics*, 20: 327–344, 1953.

J.J. Moreau. Some numerical methods in multibody dynamics: application to granularmaterials. *European Journal of Mechanics A/Solids*, 13: 93–114, 1994.

M. Nagurka and S. Huang. A mass-spring-damper model of a bouncing ball. *Int. J. Engng Ed.*, 22: 393–401, 2006.

H.A. Navarro and M.P. de Souza Braun. Linear and nonlinear Hertizian contact models for materials in multibody dynamics. In *Proceedings of the 22nd Int. Congress of Mechanical Engineering (COBEM 2013) November 3–7, 2013, Ribeirao Preto, SP, Brazil*, pages 159–180, 2013.

E. Olsson and P.-L. Larsson. On the effect of particle size distribution in cold powder compaction. *Journal of Applied Mechanics*, 79: 1–8, 2012.

J.P. Plassiard, N. Belheine, and F.V. Donze. A spherical discrete element model: calibration procedure and incremental response. *Granular Matter*, 11: 293–306, 2009.

D.O. Potyondy and P.A. Cundall. A bonded-particle model for rock. *Int. J. Rock Mech. Min. Sci.*, 41: 1329–1364, 2004.

M. Raous. Quasistatic signorini problem with Coulomb friction and coupling to adhesion. In P. Wriggers and P. Panagiotopoulos, editors, *New Developments in Contact Problems*, pages 101–178. Springer, 1999.

A. Di Renzo and F.P. Di Maio. Comparison of contact–force models for the simulation of collisions in DEM-based granular flow codes. *Chemical Engineering Science*, 59: 525–541, 2004.

D.C. Richardson, K.J. Walsh, N. Murdoch, and P. Michel. Numerical simulations of granular dynamics: I. Hard-sphere discrete element method and tests. *Icarus*, 212: 427–437, 2011.

J. Rojek. Discrete element thermomechanical modelling of rock cutting with valuation of tool wear. *Computational Particle Mechanics*, 1: 71–84, 2014.

J. Rojek, E. Oñate, F. Zarate, and J. Miquel. Modelling of rock, soil and granular materials using spherical elements. In *2nd European Conference on Computational Mechanics ECCM-2001*, Cracow, 26-29 June, 2001.

J. Rojek, F. Zarate, C. Agelet de Saracibar, Ch. Gilbourne, and P. Verdot. Discrete element modelling and simulation of sand mould manufacture for the lost foam process. *Int. J. Num. Meth. Eng.*, 62: 1421–1441, 2005.

J. Rojek, E. Onate, C. Labra, and H. Kargl. Discrete element simulation of rock cutting. *International Journal of Rock Mechanics and Mining Sciences*, 48: 996–1010, 2011.

J. Rojek, C. Labra, O. Su, and E. Oñate. Comparative study of different discrete element models and evaluation of equivalent micromechanical parameters. *Int. J. Solids and Structures*, 49: 1497–1517, 2012.

J. Rojek, G.F. Karlis, L.J. Malinowski, and G. Beer. Setting up virgin stress conditions in discrete element models. *Computers and Geotechnics*, 48: 228–248, 2013.

L. Rothenburg and R. J. Bathurst. Micromechanical features of granular materials with planar elliptical particles. *Geotechnique*, 42 (1): 79–95, 1992.

R. Senapati and J. Zhang. Identifying fracture origin in ceramics by combination of nondestructive testing and discrete element analysis. In *AIP Conference Proceedings*, volume 1211, pages 1445–1451, 2010.

M. Shillor, M. Sofonea, and J.J. Telega. *Models and Analysis of Quasistatic Contact. Variational Methods*. Lect. Notes Phys. 655, Springer, 2004.

B. Storåkers, S. Biwa, and P.-L. Larsson. Similarity analysis of inelastic contact. *Int. J. Solids and Structures*, 34: 3061–3083, 1997.

B. Storåkers, N.A. Fleck, and R.M. McMeeking. The viscoplastic compaction of composite powders. *Journal of the Mechanics and Physics of Solids*, 47: 785–815, 1999.

H. Tao, W. Zhong, and B. Jin. Flow behavior of non-spherical particle flowing in hopper. *Frontiers in Energy*, 3: 315–321, 2014.

L.M. Taylor and D.S. Preece. Simulation of blasting induced rock motion. *Eng. Comput.*, 9 (2): 243–252, 1992.

C. Thornton. Coefficient of restitution for collinear collisions of elastic-perfectly plastic spheres. *J. Appl. Mech*, 64: 383–386, 1997.

Y. Tsuji, T. Tanaka, and T. Ishida. Lagrangian numerical simulation of plug flow of cohesionless particles in a horizontal pipe. *Powder Technology*, 71: 239–250, 1992.

L. Vu-Quoc, X. Zhang, and L. Lesburg. A normal force-displacement model for contacting spheres accounting for plastic deformation: Force-driven formulation. *Journal of Applied Mechanics*, 67: 363–371, 2000.

O.R. Walton. Explicit particle dynamics for granular materials. In *Proc. 4th Int. Conf. on Numerical Methods in Geomechanics*, pages 1261–1268, Eldmonton, Canada, 1982.

O.R. Walton. Particle dynamics calculations of shear flow. In J.T. Jenkins and M. Satake, editors, *Mechanics of Granular Materials: New Models and Constitutive Relations*, pages 327–338. Elsevier, 1983.

O.R. Walton and R.L. Braun. Stress calculations for assemblies of inelastic spheres in uniform shear. *Aeta Mechanica*, 63: 73–86, 1986.

Y. Wang, F. Alonso-Marroquin, and W.W. Guo. Rolling and sliding in 3-D discrete element models. *Particuology*, 23: 49–55, 2015.

T. Wanne. *Bonded-particle modeling of thermally induced damage in rock*. PhD thesis, University of Toronto, 2009.

L. Widuliński, J. Kozicki, and J. Tejchman. Numerical Simulations of Triaxial Test with Sand Using DEM. *Archives of Hydro-Engineering and Environmental Mechanics*, 56: 149–171, 2009.

J.R. Williams, G. Hocking, and G.G.W. Mustoe. The theoretical basis of the discrete element method. In *NUMETA 1985, Numerical Methods of Engineering, Theory and Applications*. A.A. Balkema, Rotterdam, 1985.

T. Wu, I. Temizer, and P. Wriggers. Computational thermal homogenization of concrete. *Cement and Concrete Composites*, 35: 59–70, 2013.

E. Zdancevičius, R. Kačianauskas, and D. Zabulionis. Improvement of viscoelastic damping for the Hertz contact of particles due to impact velocity. *Procedia Engineering*, 172: 1286–1290, 2017.

H.W. Zhang, Q. Zhou, H.L. Xing, and H. Muhlhaus. A DEM study on the effective thermal conductivity of granular assemblies. *Powder Technology*, 205: 172–183, 2011.

L.F.C. Zonetti, A.S.S. Camargo, J. Sartori, D.F. de Sousa, and L.A.O. Nunes. A demonstration of dry and viscous damping of an oscillating pendulum. *Eur. J. Phys.*, 20: 85–88, 1999.

A. Zubelewicz and Z. Mroz. Numerical simulation of rock burst processes treated as problems of dynamic instability. *Rock Mechanics and Rock Engineering*, 16: 253–274, 1983.